

Syn-deformational melt percolation through a high-pressure orthogneiss and the exhumation of a subducted continental wedge (Orlica-Śnieżnik Dome, NE Bohemian Massif)

Carmen Aguilar, Pavla Štípská, Francis Chopin, Karel Schulmann, Pavel Pitra, Prokop Závada, Pavlína Hasalová, Jean-Emmanuel Martelat

▶ To cite this version:

Carmen Aguilar, Pavla Štípská, Francis Chopin, Karel Schulmann, Pavel Pitra, et al.. Syndeformational melt percolation through a high-pressure orthogneiss and the exhumation of a subducted continental wedge (Orlica-Śnieżnik Dome, NE Bohemian Massif). International Journal of Earth Sciences, 2020, 109 (4), pp.1213-1246. 10.1007/s00531-020-01838-4. insu-02528975

HAL Id: insu-02528975 https://insu.hal.science/insu-02528975

Submitted on 2 Apr 2020 $\,$

HAL is a multi-disciplinary open access archive for the deposit and dissemination of scientific research documents, whether they are published or not. The documents may come from teaching and research institutions in France or abroad, or from public or private research centers. L'archive ouverte pluridisciplinaire **HAL**, est destinée au dépôt et à la diffusion de documents scientifiques de niveau recherche, publiés ou non, émanant des établissements d'enseignement et de recherche français ou étrangers, des laboratoires publics ou privés.

- ¹ Syn-deformational melt percolation through a high-pressure orthogneiss and the
 ² exhumation of a subducted continental wedge (Orlica-Śnieżnik Dome, NE Bohemian
 ³ Massif)
- ⁴ Carmen Aguilar^{a*}, Pavla Štípská^{a,b}, Francis Chopin^{a,b}, Karel Schulmann^{a,b}, Pavel Pitra^{a,c},
 ⁵ Prokop Závada^d, Pavlína Hasalová^a, Jean-Emmanuel Martelat^e
- ^a Centre for Lithospheric Research, Czech Geological Survey, Klárov 3, CZ-11821 Prague,
- 7 Czech Republic
- 8 ^b Université de Strasbourg, CNRS, IPGS UMR 7516, 1 rue Blessig, F-67000 Strasbourg
- 9 Cedex, France
- ^c Univ Rennes, CNRS, Géosciences Rennes, UMR 6118, 35000 Rennes, France
- ^d Institute of Geophysics, Academy of Sciences, Boční II/1401, CZ–14131 Prague, Czech
 Republic.
- ¹³ ^e Laboratoire de Géologie de Lyon CNRS UMR5276, Université Claude Bernard et École
 ¹⁴ Normale Supérieure, F-69622 Villeurbanne, France
- 15 * *Corresponding author: <u>carmen.gil@geology.cz</u>* (C. AGUILAR)
- 16

17 ABSTRACT

18 High-pressure granitic orthogneiss of the south-eastern Orlica-Śnieżnik Dome (NE Bohemian 19 Massif) shows relics of a shallow-dipping foliation, reworked by upright folds and a mostly 20 pervasive N-S trending subvertical axial planar foliation. Based on macroscopic observations, 21 a gradual transition from banded to schlieren and nebulitic orthogneiss was distinguished. All 22 rock types comprise plagioclase, K-feldspar, quartz, white mica, biotite and garnet. The 23 transition is characterized by increasing presence of interstitial phases along like-like grain 24 boundaries and by progressive replacement of recrystallized K-feldspar grains by fine-grained 25 myrmekite. These textural changes are characteristic for syn-deformational grain-scale melt 26 percolation, which is in line with the observed enrichment of the rocks in incompatible 27 elements such as REEs, Ba, Sr, and K, suggesting open-system behaviour with melt passing 28 through the rocks. The P-T path deduced from the thermodynamic modelling indicates 29 decompression from ~15-16 kbar and ~650-740 °C to ~6 kbar and ~640 °C. Melt was already 30 present at the P-T peak conditions as indicated by the albitic composition of plagioclase in 31 films, interstitial grains and in myrmekite. The variably re-equilibrated garnet suggests that 32 melt content may have varied along the decompression path, involving successively both melt 33 gain and loss. The 6–8 km wide zone of vertical foliation and migmatite textural gradients is 34 interpreted as vertical crustal-scale channel where the grain-scale melt percolation was 35 associated with horizontal shortening and vertical flow of partially molten crustal wedge en 36 masse.

37

³⁸ **Keywords**: H*P*-granitic orthogneiss; petrological modelling; melt percolation; exhumation

39

40 INTRODUCTION

41 Recent petrological and microstructural studies show increased role of interplay between 42 grain-scale melt transfer and deformation in various tectonic settings ranging from continental 43 subduction (Závada et al. 2018), extrusion of subducted crust in continental wedges (Štípská 44 et al. 2019) and in Cordilleran magmatic arc (Stuart et al. 2018). In all these settings melt 45 passes through deforming crust exploiting grain boundaries mostly of felsic granitic protoliths 46 without segregation into veins and dykes typical for metasedimentary migmatites (Collins and 47 Sawyer, 1996; Brown and Solar, 1998; Weinberg, 1999; Vanderhaeghe, 2001). For all the 48 above mentioned studies the typical feature is connection of this pervasive grain-scale flow 49 with ductile shear zones, in particular with domains characterized by almost isotropic granite⁵⁰ like texture (Hasalová et al. 2008a). Závada et al. (2018) also suggested that prerequisite of ⁵¹ pervasive porous flow of granitic melt is granular flow or cohesion-less grain boundary ⁵² sliding of relictual parental grains enabling dynamic dilatancy of grain boundaries, typical for ⁵³ ultramylonitic cores of shear zones (Závada et al. 2007; Schulmann et al. 2008; Oliot et al. ⁵⁴ 2014).

55 Petrological studies characterizing role of melt for vertical transfer of rocks through crust 56 are scarce, but the existing studies indicate that chemistry of crystallized interstitial melt and 57 compositional variations of minerals can record exhumation of rocks of the order of ~10-20 58 kilometers (Hasalová et al. 2008b; Štípská et al. 2019; Nahodilová et al. 2020). In addition, 59 these studies indicate that dynamically moving melt plays a major role in exhuming large 60 portions of continental crust. Quantitative petrological studies of simultaneously migmatized 61 and deformed granitoids thus provide unique insight into mechanisms of exhumation of 62 deeply buried crust as proposed already by pioneering works of Hollister (1993) and Brown 63 and Solar (1998).

64 The Orlica-Śnieżnik Dome (OSD) located at the NE extremity of the Bohemian Massif 65 represents an ideal site where simultaneous deformation and melt transfer can be studied (see 66 Fig. 1). The OSD is part of a continental wedge that shows structural and petrological records 67 of continental subduction followed by vertical extrusion of partially molten deep crust in form 68 of a giant gneiss dome (Chopin et al. 2012a). The extrusion process is characterized by 69 elevation of two antiforms. The western Międzygórze antiform is marked by good 70 preservation of shallow-dipping HP subduction fabrics reworked by vertical and localized 71 melt-bearing zones, associated with heterogeneous exhumation of buried rocks (Štípská et al. 72 2019). In contrast, the eastern and larger Králíky-Śnieżnik antiform shows widespread 73 melting of the crust associated with almost complete reworking of previously subducted rocks in up to 10-kilometer-wide zone of migmatites and granitoids (Chopin et al. 2012a; Lehmann
et al. 2013).

76 Our goal is to examine a key outcrop section of the Králíky-Śnieżnik antiform where the 77 continental subduction fabrics are almost completely transposed during simultaneous 78 horizontal shortening and vertical melt transfer. On this key section, rock types range from 79 augen to banded and migmatitic orthogneiss. These rocks are studied using microstructural 80 qualitative analysis, whole-rock geochemistry and quantitative petrological modelling to 81 illustrate open-system behaviour where melt percolates through granitic protolith during 82 homogeneous crustal-scale deformation. By means of thermodynamic modelling, it will be 83 shown that homogeneous pervasive melt percolation associated with grain-scale deformation 84 contributes to the exhumation of partially molten crust en masse. We discuss homogeneous 85 deformation of crust, mineral transformations of solid phases and the mutual interactions of 86 melt with the rocks during syn-deformational melt percolation. Furthermore, we argue that 87 pervasive melt percolation is the principal mechanism controlling exhumation of deep 88 continental crust in hot collisional orogens of which the Bohemian Massif is a world example.

89 **GEOLOGICAL SETTING**

90 The OSD is considered to be a part of the high-grade Moldanubian–Lugian zone representing 91 deeply eroded Variscan orogenic root (Fig. 1a; e.g. Franke and Zelaźniewicz, 2000; 92 Aleksandrowski and Mazur, 2002). The structure of the OSD corresponds to a mantled gneiss 93 dome (e.g. Eskola, 1948) with a core formed by medium- to high-grade metamorphic rocks 94 surrounded by low-grade slates and metavolcanic rocks (Fig. 1b; e.g. Don et al. 1990; Mazur 95 and Aleksandrowski, 2001). The central part of the dome is made up by antiforms cored by 96 felsic orthogneiss with eclogite and HP granulite lenses (Kozłowski, 1961; Smulikowski, 97 1967; Pouba et al. 1985), alternating with N-S trending synforms formed mainly by 98 metasedimentary sequences (Fig. 1b). The felsic orthogneiss types are traditionally divided

99 into coarse-grained augen to banded Śnieżnik and fine-grained mylonitic to migmatitic 100 Gierałtów orthogneiss (e.g. Fischer, 1936; Lange et al. 2002; Żelaźniewicz et al. 2002; 101 Chopin et al. 2012b). The orthogneiss protolith corresponds to a granite emplaced at c. 510– 102 490 Ma within a host metasedimentary sequence (e.g. Oliver et al. 1993; Borkowska and 103 Dörr, 1998; Kröner et al. 2000; 2001; Lange et al. 2005; Bröcker et al. 2009; Mazur et al. 104 2010). The protolith age of the (U)HP granulite facies rocks remains still controversial but it 105 is probably older than c. 470 Ma (Štípská et al. 2004; Lange et al. 2005; Anczkiewicz et al. 106 2007; Bröcker et al. 2009; Bröcker et al. 2010). The metasedimentary sequences (Młynowiec 107 and Stronie formations) are dominated by Neoproterozoic to Cambro-Ordovician paragneiss 108 and micaschist sporadically interbedded with layers of varied lithologies, such as 109 metavolcanic rocks and few lenses of quartzite, graphite schist and marble (Don et al. 1990, 110 2003).

111 The metasedimentary rocks and orthogneiss together with (U)HP rocks were affected by 112 an Early Carboniferous metamorphism (c. 340 Ma; e.g. Turniak et al. 2000; Štípská et al. 113 2004; Lange et al. 2005; Anczkiewicz et al. 2007; Bröcker et al. 2009; Jastrzębski, 2009; 114 Bröcker et al. 2010; Walczak et al. 2017). The orthogneiss shows amphibolite- to eclogite-115 facies conditions with peak estimates ranging from ~20 kbar/700 °C to ~27 kbar/700-800 °C 116 (e.g. Bakun-Czubarow, 1992; Bröcker and Klemd, 1996; Klemd and Bröcker, 1999; Štípská 117 et al. 2004; Chopin et al. 2012b), whereas the metapelites preserve an amphibolite-facies 118 metamorphism reaching P-T conditions of ~5–9 kbar and ~460–650 °C (Murtezi, 2006; 119 Jastrzębski, 2009; Jastrzębski et al. 2010, 2016; Skrzypek et al. 2011a,b, 2014; Štípská et al. 120 2012). UHP metamorphism (reaching ~30 kbar) was proposed for eclogite and HP-granulite 121 (Bakun-Czubarow, 1991, 1992; Kryza et al. 1996; Klemd and Bröcker, 1999; Ferrero et al. 122 2015; Jedlička et al. 2017; Walczak et al. 2017; Majka et al. 2019), while other authors 123 suggest lower P-T conditions of ~19-22 kbar at 700-800 °C for the eclogite (Bröcker and

124 Klemd, 1996; Štípská et al. 2012) and ~18–22 kbar at 800–1000 °C for the granulite (Pouba et 125 al. 1985; Steltenpohl et al. 1993; Štípská et al. 2004; Bröcker et al. 2010; Budzyń et al. 2015). 126 Retrograde metamorphism has been estimated at ~4-9 kbar and 550-700 °C for the eclogite 127 (Klemd et al. 1995; Bröcker and Klemd, 1996; Štípská et al. 2012), and at ~8–12 kbar and 128 560-800 °C for the granulite (Steltenpohl et al. 1993; Štípská et al. 2004). Numerous cooling 129 ages at c. 350–330 Ma were obtained using Rb–Sr and 40 Ar– 39 Ar phengite and biotite dating 130 (e.g. Steltenpohl et al. 1993; Maluski et al. 1995; Białek and Werner, 2004; Lange et al. 2005; 131 Schneider et al. 2006; Anczkiewicz et al. 2007; Bröcker et al. 2009; Chopin et al. 2012a).

132 Available geological, geochronological and geophysical data allowed to divide the 133 tectonic evolution of the OSD into three main stages: (1) HP metamorphism of Late Devonian 134 - Early Carboniferous age associated with continental underthrusting of the Saxothuringian 135 crust beneath the autochthonous Teplá-Barrandian type Neoproterozoic crust (Fig. 1a,b; 136 Chopin et al. 2012b; Mazur et al. 2012; Majka et al. 2019). (2) Extrusion of a Saxothuringian-137 derived high-grade metamorphic core through the upper crust of the upper plate in front of the 138 Brunia microcontinent. This event is responsible for exhumation of HP rocks and their re-139 equilibration at mid-crustal conditions (Štípská et al. 2004, 2012; Majka et al. 2019), while 140 metasedimentary rocks were simultaneously buried in marginal synforms (Skrzypek et al. 141 2011a,b; Štípská et al. 2012; Skrzypek et al. 2014). (3) Ductile thinning event associated with 142 formation of detachments and unroofing of the apical part of the dome (Pressler et al. 2007; 143 Chopin et al. 2012a; Lehmann et al. 2013).

¹⁴⁴ The south-eastern part of the OSD

The south-eastern part of the OSD represents a type section through the extruded Saxothuringian-derived crustal portion, where structural and petrological evolution of rocks affected by vertical ductile flow can be studied (see Fig. 1b). This section consists of the gneissic Międzygórze antiform in the west and the Králíky-Śnieżnik antiform in the east,
separated from each other by a metasedimentary synform cropping out mainly in the Morava
valley (Figs. 1c and 2a; Don, 1964, 1982; Chopin et al. 2012a; Štípská et al. 2012).

151 The previously well studied Międzygórze antiform is formed by an orthogneiss cored by a 152 N-S trending belt of eclogite lenses (Figs. 1c and 2a; Chopin et al. 2012a,b; Štípská et al. 153 2012). Here, low-strain augen orthogneiss was progressively transformed into a banded to 154 migmatitic orthogneiss (Chopin et al. 2012b). The banded and migmatitic orthogneiss are the 155 most abundant in a ~1.5 km wide zone around the eclogite belt, whereas the augen 156 orthogneiss is developed east of the high-grade orthogneiss-eclogite core (see Fig. 2a). The 157 distinct textural varieties of the three orthogneiss types were interpreted as a result of 158 deformation and metamorphism of the same Cambro-Ordovician granite protolith, reflecting 159 mostly strain gradient and migmatization (Turniak et al. 2000; Lange et al. 2005; Chopin et al. 160 2012b), but also variable degree of melt-rock interaction (Štípská et al. 2019).

161 In the Międzygórze antiform, the augen orthogneiss displays a sub-horizontal S1 foliation 162 (Fig. 2a), which is deformed by asymmetrical m- to km-scale open upright F2 folds associated 163 with progressive transposition into a N-S striking subvertical S2 metamorphic foliation in the 164 banded to migmatitic orthogneiss (Chopin et al. 2012a,b; Štípská et al. 2012; 2019). Finally, 165 the S2 migmatitic foliation was heterogeneously reworked by a weakly developed F3 166 recumbent folds and rare sub-horizontal S3 axial plane cleavage (Fig. 2a). The banded to 167 migmatitic orthogneiss adjacent to the eclogite experienced prograde evolution along a HP 168 gradient reaching eclogite-facies conditions similar to that of the adjacent eclogite. This 169 implies that both lithologies shared the same process of burial to ~19-20 kbar and >700 °C 170 (Chopin et al. 2012b; Štípská et al. 2012). This contrasts with the conditions from augen 171 orthogneiss in direct continuity with paragneiss in the synforms, which show maximum burial

172 conditions of ~7.5-8.0 kbar and ~600-620 °C (Jastrzebski et al. 2017). Recent mineral 173 equilibria modelling of *Štípská* et al. (2019) reveals that the migmatitic orthogneiss types 174 were equilibrated at ~15-17 kbar and ~690-740 °C during infiltration of a granitic melt. 175 Retrograde equilibration down to \sim 7–10 kbar was largely restricted to retrograde zoning in 176 phengite, garnet and plagioclase, and crystallization of biotite around phengite and garnet. 177 Here, Early Carboniferous metamorphic ages of c. 340–360 Ma were determined on zircon 178 rims in migmatitic orthogneiss (Turniak et al. 2000; Lange et al. 2005) and on zircon in 179 leucosomes and leucocratic veins (Bröcker et al. 2009).

180 In the Morava valley metasedimentary synform, microstructural and petrological evidence 181 suggests that the S1 fabric is associated with prograde metamorphism along a MP-MT 182 gradient reaching garnet- to staurolite-grade conditions at ~6 kbar/580 °C (Štípská et al. 183 2012). A continuous growth of both garnet and staurolite parallel to S2 indicates prograde 184 metamorphism up to ~7.5 kbar/630 °C in the sub-vertical fabric. However, chlorite parallel to 185 the S2 foliation suggests that retrograde metamorphism and exhumation to ~5 kbar/500 °C 186 also occurred during this deformation event. The P-T path related to D3 was a prolonged 187 retrograde evolution towards temperature lower than 550 °C (Štípská et al. 2012).

188 In the eastern N-S trending Králíky-Śnieżnik antiform, the augen to banded mylonitic 189 orthogneiss is rare and the bulk of the antiform is formed by a migmatitic orthogneiss. 190 Eclogite lenses occur in places in the migmatitic orthogneiss and in the north the core of the 191 antiform is formed by intermediate to felsic HP granulites (Fig. 1c; Pouba et al. 1985; Štípská 192 et al. 2004). The whole Králíky-Śnieżnik antiform is characterized by significantly higher 193 degree of migmatization compared to the westerly Międzygórze antiform (Figs. 1c and 2b). 194 Recent petrological studies from the granulite belt indicate UHP conditions of ~20-25 kbar 195 and ~550-950 °C (Budzyń et al. 2015; Jedlička et al. 2017; Walczak et al. 2017) which is 196 consistent with melt inclusion study from felsic granulites that show trapping conditions for melt at ~27 kbar and ~875 °C, suggesting near UHP conditions of melting (Ferrero et al.
2015). The age of metamorphism is constrained by U–Pb dating of zircon to *c*. 340 Ma
(Štípská et al. 2004; Walczak et al. 2017).

200 In the Králíky-Śnieżnik antiform, the rare relics of the earliest S1 fabric are systematically 201 related to various types of migmatitic orthogneiss. These structures are mostly transposed by 202 the dominant N-S sub-vertical S2 foliation (Fig. 2b). The whole domain is characterized by 203 decimetre-scale transitions from remnants of partially molten porphyritic 'augen' to 'banded' 204 orthogneiss and finally, to 'fine-grained' migmatitic orthogneiss (Figs. 1c and 2b; Don, 1982; 205 Chopin et al. 2012a). This type of transition is classically referred to as the Śnieżnik augen 206 gneiss - Gierałtów gneiss transition in the whole OSD (Lange et al. 2002 and references 207 therein). However, this distinction is descriptive and only rarely took into account the 208 processes leading to the gradual development of these rock types (Chopin et al. 2012a,b; 209 Štípská et al. 2012).

210 FIELD RELATIONS AND STRUCTURAL EVOLUTION

211 Field relations and textural types of the orthogneiss were examined along a representative 212 outcrop in the central part of the Králíky-Śnieżnik antiform (UTM WGS84 coordinates 50° 5' 213 37.54"N and 16° 51' 12.90"E; Figs. 1c, 2b and 3a). Here, the orthogneiss shows 214 macroscopically a range of textures with continuous transitions among them (see Fig. 3b-f). 215 In description of different rock types, we follow *Štípská* et al. (2019): we use the term augen 216 or banded type I where the augen/bands of recrystallized quartz, plagioclase and/or K-feldspar 217 have sharp boundaries and appear macroscopically monomineralic; the term augen or banded 218 type II where the recrystallized K-feldspar augen/bands appear macroscopically 219 monomineralic, but have diffuse boundaries, and bands of quartz and plagioclase are ill 220 defined; the term schlieren for rock types with polymineralic and/or monomineralic, felsic and/or mafic bands elongated parallel to foliation within a nearly isotropic matrix; and nebulitic for rock types with nearly homogeneous distribution of phases. The studied outcrop is dominated by banded type II, schlieren and nebulitic orthogneiss (see Fig. 3b–f). Because of continuous transitions among the rock types, it is sometimes difficult to assign each sample unequivocally to a single rock type, and also, looking at rocks at different scale may lead to assigning them to different types (e.g. schlieren and nebulitic in Fig. 3e,f).

227 The S1 foliation is tightly folded by cm- to dm-scale upright close to isoclinal F2 folds 228 with N-S trending subhorizontal axes and subvertical N-S trending axial planes (Fig. 3a,c,d). 229 The intersection lineation L2 is parallel to the F2 fold hinges (Fig. 2b). This upright folding 230 locally results in formation of N-S striking subvertical S2 axial planar cleavage (Fig. 3d). 231 Here, the foliation in limbs of the isoclinal folds appear in subvertical position, subparallel to 232 the S2 cleavage, and therefore the foliation in these limbs represents a composite S1-2 233 foliation (Fig. 3c,d). Rock types in the S1 foliation occurring mainly in the F2 limbs are 234 represented by banded type II orthogneiss (e.g. Fig. 3b,c,d). Rock types in the cleavage are 235 represented mainly by schlieren and nebulitic orthogneiss (e.g. Fig. 3e). In areas where only 236 the subvertical fabric is present, the rock transitions from banded type II to schlieren and 237 nebulitic orthogneiss are most typical (Fig. 3f).

238 In order to put valorisation to the field observations, we make here some basic 239 interpretation of the observed textural transitions (for similar interpretation see Hasalová et al. 240 2008a,b,c; Schulmann et al. 2008; Chopin et al. 2012b; Štípská et al. 2019). From the gradual 241 transitions of the rock types in the field, it is concluded that the banded type II, schlieren and 242 nebulitic orthogneiss types resulted from progressive disappearance of the originally 243 monomineral augen/banded texture typical of the augen/banded type I orthogneiss. From the 244 observed textural gradients occurring parallel to the S2 foliation and ranging from the banded 245 type II to schlieren and nebulitic orthogneiss types, it is concluded that these transformations occurred mainly during the D2 deformation. As the schlieren and nebulitic textures are
commonly assigned to migmatites (Mehnert, 1971), it is supposed that the observed textural
transitions are a result of transformation under the presence of melt (for similar interpretation
see also Hasalová et al. 2008a,b,c; Schulmann et al. 2008; Chopin et al. 2012b; Závada et al.
2018; Štípská et al. 2019).

251 MICROSTRUCTURAL AND PETROGRAPHIC FEATURES

252 Microstructural and petrological studies were carried out on 10 samples collected along the 253 outcrop section (see Fig. 3a for location of samples). Characterization of the different 254 orthogneiss types was carried out by combining optical microscopy, back-scattered electron 255 imaging (BSE) and optical cathodoluminescence (CL) on XZ oriented thin sections (Figs. 4 256 and 5). BSE images were acquired by a Tescan VEGA\\XMU electron microscope at the 257 Charles University in Prague (Czech Republic). The CL mosaics were compiled from around 258 90-250 images that were captured using the CITL Mk5-2 CL microscope at 700 mA with a 259 capture time of 1.5 s at the Czech Geological Survey in Prague.

In all the rock types, the mineral assemblage is plagioclase, K-feldspar, quartz, white mica, biotite and garnet. Apatite and zircon are present as accessory minerals in the matrix, ilmenite is only enclosed in biotite. Mineral abbreviations used here are: ksp, K-feldspar; pl, plagioclase; q, quartz; bi, biotite; g, garnet; ap, apatite; ilm, ilmenite; myr, myrmekite (mainly after Holland and Powell, 1998). White mica (wm) is used in diagrams because the composition ranges from phengite (ph) to muscovite (mu). Phengite is used where the observed white mica has phengitic composition.

In the following microstructural descriptions, we characterize the spatial distribution of K feldspar, plagioclase, quartz and micas in individual rock types (Fig. 4a–d).

²⁶⁹ Banded type II orthogneiss

270 At microscopic scale, this rock type is characterized by alternation of K-feldspar, quartz and 271 plagioclase-rich layers or domains. The boundaries between individual layers range from 272 sharp (e.g. white arrows in Fig. 3b and Fig. 4a) to diffuse (e.g. Fig. 4b). The K-feldspar-rich 273 layers have an interconnected network of K-feldspar grains separated by ~5% (e.g. Fig. 4a) up 274 to ~20% (e.g. Fig. 4b) of interstitial quartz, plagioclase and myrmekite. The quartz-rich layers 275 are composed of interconnected grains of quartz with ~5% up to 30% of interstitial feldspar, 276 white mica, biotite, garnet and accessory minerals (e.g. Fig. 4a,b). The plagioclase-rich layers 277 are thinner and more irregular compared to the K-feldspar and quartz-rich layers and have up 278 to 30% of interstitial quartz, K-feldspar, white mica, biotite, garnet and accessory minerals in 279 some samples (e.g. Fig. 4a), while in other samples only ill-defined plagioclase-rich domains 280 with up to 50% of other phases are identified (Fig. 4b).

281 K-feldspar grains in K-feldspar-rich layers are slightly elongated, with irregular shape and 282 50-1000 µm in size (Fig. 5a). Large grains of K-feldspar show a well-developed shape 283 preferred orientation parallel to the macroscopic foliation, whereas preferred orientation of 284 smaller grains is less developed (Fig. 5a). The boundaries between elongated K-feldspar 285 grains are serrated and lined by irregular <10-30 µm wide films of plagioclase, irregular 286 plagioclase grains 10-300 µm in size and by rounded quartz grains 10-500 µm in size. K-287 feldspar grains show cuspate-lobate boundaries with respect to interstitial plagioclase and 288 quartz (Fig. 5b). Small myrmekite-like aggregates 10–200 µm in size are also present along 289 the K-feldspar grains within the K-feldspar-rich layers (Fig. 5b). Myrmekite is composed 290 mostly of fine-grained plagioclase and quartz, with small and rare grains of K-feldspar and 291 white mica.

²⁹² Plagioclase aggregates have granoblastic microstructure and an average grain size of 400 ²⁹³ μ m. The plagioclase grains do not display a visible shape preferred orientation (Fig. 5c). The ²⁹⁴ rounded and isolated quartz (10–100 μ m) and cuspate small K-feldspar (10–50 μ m in size)

²⁹⁵ occur as interstitial grains at triple junctions of the plagioclase grains. Boundaries between ²⁹⁶ plagioclase grains are mostly irregular. In addition, layers rich in polygonal plagioclase ²⁹⁷ (1500–2500 μ m) with antiperthite core are locally observed parallel to the S2 foliation (Fig. ²⁹⁸ 5d).

Quartz forms recrystallized aggregates composed of large and inequigranular grains
 30–2000 µm in size with amoeboid to highly lobate boundaries (Fig. 4a,b). They show a
 weak shape preferred orientation. Feldspar crystals penetrate heterogeneously into quartz
 aggregates along mutually lobate boundaries (Fig. 5c).

303 Schlieren orthogneiss

304 At microscopic scale, the schlieren are composed mostly by relict K-feldspar-rich domains 305 with up to 40% of interstitial phases. The K-feldspar-rich domains have very irregular 306 boundaries with the surrounding matrix (see white-dashed lines in Fig. 4c). The internal 307 textures within these K-feldspar-rich domains are identical to the textures described for the 308 banded type II orthogneiss and are mainly characterized by cuspate-lobate boundaries of K-309 feldspar grains with respect to interstitial plagioclase, quartz, and myrmekite (see above). The 310 matrix has nearly homogeneous distribution of all the phases typical of nebulitic texture, and 311 is described below.

312 Nebulitic orthogneiss

This rock type is characterized by nearly homogeneous distribution of all the phases. Kfeldspar, plagioclase and quartz grains are highly irregular and show large variation in grain size from <1 μ m up to 1.5 mm (Figs. 4c,d and 5e). The larger grains of K-feldspar are surrounded by abundant myrmekite. Locally, K-feldspar has at its rim quartz-white mica symplectite when it occurs at contact with white mica (Fig. 5f).

³¹⁸ Textural relations of white mica, biotite and garnet

319 In the banded type II orthogneiss, both white mica and biotite tend to form aggregates or also 320 occur as individual grains within the layers dominated by plagioclase and quartz, and are 321 strongly to weakly oriented parallel to the S1-2 foliation (Fig. 5c). In the schlieren and 322 nebulitic orthogneiss, micas tend to appear as individual grains that are strongly oriented 323 parallel to the S2 foliation (Fig. 5e). The proportion of white mica is higher compared to 324 biotite (around 70% and 30% of all micas respectively). However, the amount of biotite is 325 higher in the banded type II, and lower in the schlieren and nebulitic orthogneiss (reaching 326 $\sim 40\%$, $\sim 30\%$ and 20% of the total amount of the micas, respectively). White mica forms 327 commonly large laths (250–1000 µm in size) with small or large biotite at its margins, along 328 its cleavage or in its crystallographic continuity (Fig. 5g). These features indicate that this 329 biotite grew at the expense of white mica. Biotite is partially or completely chloritized. Garnet 330 (<2 vol. %) occurs as small grains (around 50–200 µm) inside plagioclase or quartz, or as 331 small (up to 500 µm) grains at contact with plagioclase and quartz, but in some places it is 332 also in contact with white mica and biotite. Garnet has irregular shapes and is commonly 333 fragmented (Fig. 5e).

From the observation at microscale, we conclude that the progressively higher amount of interstitial phases observed along like-like grain boundaries from the banded type II, to schlieren and to nebulitic orthogneiss is responsible for progressive disintegration of originally monomineral layers typical of weakly migmatized banded type II orthogneiss (Fig. 4a–d). The nucleation of interstitial phases is typically explained by crystallization from melt (for identical interpretation of similar rock sequence see also Hasalová et al. 2008a,b,c; Schulmann et al. 2008; Chopin et al. 2012b; Štípská et al. 2019).

341 MINERAL CHEMISTRY

342 Samples corresponding to different orthogneiss types were selected for mineral chemical
 343 analysis. Minerals were analysed using the *Electron Probe Micro-Analyser* (EPMA) JEOL

344 8200 at the University of Lausanne (Switzerland) and Jeol FEG-EPMA JXA-8530F at the 345 Charles University in Prague (Czech Republic). The analyses were made in point beam mode 346 at 15-kV acceleration voltage and 20-nA beam current, with a spot diameter of 5 µm and a 347 counting time of 20–30 s. Representative analyses of feldspar, micas and garnet are presented 348 in Tables 1, 2 and 3 and shown in Figures 6–9. Abbreviations used for mineral end-members 349 in molar proportions are an = Ca/(Ca+Na+K); ab = (Na/(Ca+Na+K); or = K/(Ca+Na+K); X_{Fe} 350 $(ph, bi, g) = Fe_{total}/(Fe_{total} + Mg); alm = Fe^{+2}/(Fe^{+2} + Mg + Ca + Mn); sps = Mn/(Fe^{+2} + Mg)$ 351 +Ca + Mn); grs = Ca/(Fe⁺² + Mg + Ca + Mn) and prp = Mg/(Fe⁺² + Mg + Ca + Mn). The sign 352 " \rightarrow " indicates a trend in mineral composition or zoning, the sign "-" depicts a range of 353 mineral compositions and p.f.u. is per formula unit.

354 Feldspar

Recrystallized K-feldspar has subtle zoning within all the orthogneiss types (Fig. 6a–f, Table 1), with cores more albite-rich (or = 0.86-0.90; ab = 0.10-0.14) compared to rims (or = 0.90-0.94; ab = 0.06-0.10). K-feldspar in small grains in myrmekite (Fig. 6a–c), and K-feldspar forming thin films or small interstitial grains in the layers dominated by plagioclase and quartz has a lower content of albite (or = 0.92-0.96; ab = 0.04-0.08) (Fig. 6a, b).

360 Two distinct plagioclase populations have been measured according to their 361 microstructural position (Fig. 6a-f, Table 1). Plagioclase aggregates exhibit homogeneous 362 oligoclase composition (an = 0.12-0.17; ab = 0.83-0.88), whereas more sodic composition 363 (an = 0.02-0.05; ab = 0.95-0.98) is found in small interstitial plagioclase grains and thin films 364 coating the K-feldspar aggregates of the banded type II and schlieren orthogneiss (Fig. 6a). 365 Oligoclase (an = 0.12-0.22; ab = 0.78-0.88) and albite (an = 0.02-0.09; ab = 0.91-0.98) 366 compositions are also found in myrmekite-like aggregates within all the rock types (Fig. 6e, 367 **f**).

³⁶⁸ Micas

White mica shows in all rock types zoning from core to rim, with decreasing Si from $\sim 3.20-3.40$ p.f.u. to $\sim 3.10-3.20$ p.f.u., Ti from $\sim 0.03-0.08$ p.f.u. to $\sim 0.01-0.03$ p.f.u. and with increasing $X_{\text{Fe(tot)}}$ from $\sim 0.50-0.55$ to > 0.55 (Fig. 7a–d, Table 2). F content varies from 0.04 to 0.14 p.f.u. with higher values in the core (Fig. 7c, Table 2).

Biotite has similar compositional ranges in all the rock types: in banded type II orthogneiss, Ti = 0.05–0.20 p.f.u., Al = 1.65–1.95 p.f.u., $X_{Fe} = 0.74-0.78$ and F = 0.10–0.25 p.f.u.; in schlieren orthogneiss, Ti = 0.05–0.12 p.f.u., Al = 1.75–1.90 p.f.u., $X_{Fe} = 0.75-0.78$ and F = 0.10–0.20 p.f.u.; and in nebulitic orthogneiss, Ti = 0.12–0.20 p.f.u., Al = 1.65–1.75 p.f.u., $X_{Fe} = 0.76-0.78$ and F = 0.10–0.20 p.f.u. (Fig. 8, Table 2).

378 Garnet

379 Garnet exhibits a flat or significant compositional zoning in samples of banded type II to 380 schlieren orthogneiss (Fig. 9a-c, Table 3), whereas in samples of the nebulitic orthogneiss 381 garnet displays a strong zoning (Fig. 9d, Table 3). In banded type II to schlieren orthogneiss, 382 some garnet shows flat profiles with high X_{Fe} (0.95–0.98) and almandine (alm_{0.65–0.72}), low 383 pyrope $(prp_{0.02-0.04})$, grossular $(grs_{0.07-0.09})$ and spessartine $(sps_{0.10-0.19})$ (Fig. 9a-c, Table 3). In 384 some garnets of the banded type II to schlieren orthogneiss, grossular decreases ($grs_{0.18\rightarrow0.09}$) 385 and spessartine increases ($sps_{0.09\rightarrow0.19}$) from core to rim (Fig. 9a–c, Table 3). In the nebulitic 386 orthogneiss, garnet has higher grossular and lower spessartine in the core compared to banded 387 type II and schlieren orthogneiss, and garnet zoning is from core to rim marked by decrease in 388 grossular (grs_{0.34 \rightarrow 0.09}) and increase in almandine (alm_{0.59 \rightarrow 0.68}) and spessartine (sps_{0.04 \rightarrow 0.21),} 389 and accompanied by a flat trend in high X_{Fe} (0.95–0.98) and low pyrope (prp_{0.02–0.04}) (Fig. 9d, 390 Table 3).

391 WHOLE-ROCK CHEMISTRY

Whole-rock major- and trace-element analyses were performed by *Inductively Coupled Plasma-Atomic Emission Spectroscopy* (ICP-AES) and *-Mass Spectrometry* (ICP-MS) at the Acme laboratories of Canada for each rock type. Analyses are summarized in Table 4 and presented in a series of isocon diagrams (Fig. 10a,b; Grant, 1986) and spider plot normalized to Chondrite (Evensen et al. 1978) to show geochemical variations for different rock types (Fig. 10c).

398 The isocon diagrams point to weak variations of major elements for all the schlieren 399 orthogneiss (Fig. 10a) and a nebulitic orthogneiss (Fig. 10b), as were typically reported from 400 deformed and migmatized granitic rocks (Chopin et al. 2012b; Závada et al. 2018). The trace-401 element concentrations of individual rock types are compared to different rock groups 402 described by Chopin et al. (2012b) in Figure 10c. According to Chopin et al. (2012b), the 403 LREE (La, Ce, Pr and Nd) and MREE (Sm, Eu and Gd) contents drop slightly in the sequence 404 from augen to banded and mylonitic/migmatitic orthogneiss, whereas the HREE distribution 405 is homogeneous (see shaded fields in Fig. 10c). For studied rocks, the character of distribution 406 patterns for all studied samples is fairly homogeneous, showing similar REE contents 407 (~ $\Sigma REE = 55-89$ ppm., Table 4) and subparallel distribution patterns except in the nebulitic 408 orthogneiss (sample FC076C, Fig. 10c). The nebulitic orthogneiss is slightly depleted in 409 LREE and MREE and enriched in HREE compared to the banded type II and schlieren 410 orthogneiss (see red diamonds in Fig. 10c). In general, the REE compositional ranges overlap 411 the mylonitic/migmatitic group described by Chopin et al. (2012b), characterized by 412 pronounced negative Eu anomalies (Fig. 10c). This fact indicates that the studied samples can 413 be explained by increasing degree of percolating melt fractionation as was described by 414 Hasalová et al. (2008b) and Chopin et al. (2012b).

In Figure 10d, a compositional variation between the different rock types is presented in the spider plot normalized by a weakly migmatized banded type II orthogneiss (sample FC076A). Here, the character of distribution patterns for all rock types shows only slight
differences in chemical composition. According to Lange et al. (2002) and Chopin et al.
(2012b), slight differences in major and trace elements between individual rock types may be
likely due to original heterogeneity of the protolith. On the other hand, Marquer and Burkhard
(1992) and Hasalová et al. (2008b) attributed these variations to the presence of external
fluids or melt in similar felsic rocks.

423 To identify the mass transfers related to melt and/or fluid flux through the studied rock 424 types, mass balance calculations of incompatible elements have been performed using the 425 normalized Potdevin diagram for the comparison of weakly and strongly migmatized 426 orthogneiss (see Fig. 11a-c and Table 5). In this diagram, relative element transfers between 427 the selected rock types – typically a protolith and the altered rock – is conveniently expressed 428 using the relative abundance of specific element (i) and F_v volume factor (Potdevin and 429 Marquer, 1987; López-Moro, 2012). While the F_v is given by the volume ratio between the 430 transformed rock and the initial one, the difference in relative abundance of specific element 431 (i) is expressed by:

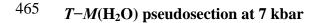
432
$$\Delta m_i = F_v (\rho_a / \rho_0) C_a^i - C_0^i$$

⁴³³ where Δm_i is the relative gain or loss of mass, and C_0^{i} and C_a^{i} are the initial and final ⁴³⁴ concentrations and ρ_0 and ρ_a the densities of these rocks, respectively.

Resulting calculations show a slight gain in a range of incompatible elements, such as
REEs, Ba, Sr, and K in banded type II (sample FC076E) and schlieren orthogneiss (sample
FC076J) (Fig. 11a–b) with respect to weakly migmatized banded type II orthogneiss (sample
FC076A). This trend is coupled with a slight loss in HFSE's, such as U, Zr, Nb, Hf and Ta.
Enrichment in REEs, Ba, Sr, and loss of HFSE's is less significant in the nebulitic
orthogneiss, which is marked mainly by depletion in Th, Cs, Pr, La, U and Ta (Fig. 11c).

441 FORWARD MODELLING OF MIGMATITIC ORTHOGNEISS

442 In the modelling of anatexis of granitic rocks at eclogite-facies conditions we follow the 443 approach discussed in Štípská et al. (2019). The assemblages are modelled metastable with 444 respect to the stability of clinopyroxene, as clinopyroxene is commonly absent in quartzo-445 feldspathic rocks at (U)HP conditions (e.g. Young and Kylander-Clark, 2015). The 446 haplogranitic melt model is used as it can explain well mineral equilibria in quartzo-447 feldspathic rocks at HP-HT conditions, even if it was not calibrated explicitly for these 448 conditions (Štípská et al. 2008; Hopkins et al. 2010; Lexa et al. 2011; Nahodilová et al. 2014). 449 Pseudosections were calculated using THERMOCALC 3.33 (Powell et al. 1998; version 450 2009) and dataset 5.5 (Holland and Powell, 1998; January 2006 upgrade), in the system MnO-451 Na₂O-CaO-K₂O-FeO-MgO-Al₂O₃-SiO₂-H₂O-TiO₂-O (MnNCKFMASHTO). The activity-452 composition relationships used are as follows: for silicate melt (liq), from White et al. (2007); 453 for garnet (g), biotite (bi) and ilmenite (ilm), from White et al. (2005); for feldspar (pl, ksp), 454 from Holland and Powell (2003); for white mica (wm), from Coggon and Holland (2002); 455 and, for cordierite (cd), from Holland and Powell (1998). The calculations are done for the 456 whole-rock composition of a nebulitic orthogneiss (sample FC076C; Table 4). Because of 457 closely similar whole-rock compositions of the other samples (Fig. 10b) the calculated 458 diagrams are also used for interpretation of their metamorphic evolution. The amount of H₂O 459 in the whole-rock composition was deduced from $T-M(H_2O)$ pseudosection (see description 460 below, Fig. 12). Mineral composition isopleths of garnet, white mica, plagioclase and molar 461 proportion of liquid were plotted to discuss P-T conditions of mineral equilibration. The 462 isopleth notation used is: m(sps) = Mn/(Ca+Mg+Fe+Mn)*100;x(alm) =463 Fe/(Ca+Mg+Fe+Mn)*100; z(grs) = Ca/(Ca+Mg+Fe+Mn)*100; Si(wm) p.f.u.; ca(pl) = Ca/(Ca+Mg+Fe+Mn)464 Ca/(Ca+Na+K) and liq (mol. %).



466 In order to estimate the conditions of last equilibration in migmatites, it is assumed that the 467 assemblage tends to equilibrate until it becomes melt poor or melt absent near or at the solidus 468 (e.g. Štípská and Powell, 2005; Hasalová et al. 2008c). Therefore, a $T-M(H_2O)$ pseudosection 469 at a pressure of 7 kbar was calculated first, simulating conditions of last equilibration with 470 melt near the solidus (Fig. 12). The observed assemblage of q-pl-ksp-g-bi-wm-ilm-liq is 471 stable at $T-M(H_2O) = -0.30-0.53$ and at -630-710 °C and the observed garnet rim 472 composition (~alm₆₈; grs₁₀; sps₂₀) fits the calculated isopleths at conditions of $T-M(H_2O) =$ 473 ~0.52 and ~630 °C (Fig. 12). Therefore, it is assumed that the rocks crossed the solidus with 474 minimum H₂O content corresponding to 2.07 mol. % of H₂O in the whole-rock composition.

475

Closed-system *P*–*T* pseudosection

476 The *P*–*T* diagram (Fig. 13) was calculated for an amount of $H_2O = 2.07$ mol. % deduced from 477 the $T-M(H_2O)$ diagram (see Fig. 12 and related discussion). This H₂O amount allows the 478 stability of a typical mineral assemblage of a granite at MP-MT conditions, which is H₂O-479 free and garnet-free (~5.2-6.7 kbar and <550-620 °C), and therefore may illustrate rock 480 evolution in a closed system, even for H₂O. The major features and topology of the diagram 481 involve a H_2O -saturated solidus up to ~7.8 kbar followed by a steeply inclined H_2O -482 undersaturated solidus from ~7.8 kbar to higher pressure at progressively higher temperature. 483 The biotite-out and garnet-out lines are temperature sensitive at suprasolidus and subsolidus 484 conditions, respectively and pressure sensitive at subsolidus conditions (Fig. 13).

The resulting *P*–*T* phase diagram shows a stability field of q-pl-ksp-g-bi-wm-ilm-liq between ~4–12 kbar and ~630–740 °C, corresponding to the observed assemblage in all the rock types. The nebulitic orthogneiss preserves high grossular content of garnet in the core (alm_{60-65} ; grs_{30-34} ; sps_4 ; Fig. 9d), pointing to a *P*–*T* peak in the melt-free stability field of q-plksp-g-bi-wm-ru at ~14–16 kbar and ~600–740 °C (ellipse 1 in Fig. 13a–b). The high Si content in white mica in all the rock types (Si = 3.35–3.40 p.f.u.; Fig. 7a) supports its 491 crystallization at high pressure conditions at ~16 kbar (Fig. 13c). The plagioclase composition 492 measured in films and interstitial grains is albite $(an_{0.05-0.02}; ab_{0.95-0.98})$, compatible with 493 plagioclase crystallization at HP conditions at ~16 kbar (Fig. 13d). The presence of interstitial 494 plagioclase, quartz and K-feldspar is interpreted as crystallized from melt at grain boundaries 495 (e.g. Hasalová et al. 2008a). We documented also albite and oligoclase composition in 496 myrmekite-like aggregates. According to Barker (1970), the myrmekite is typically associated 497 with higher anorthite content in plagioclase then observed in this study or other similar studies 498 (Štípská et al. 2019). The albite compositions measured in myrmekite may be result of the 499 presence of melt at HP conditions, and partial reequilibration of plagioclase to oligoclase on 500 decompression. The oligoclase compositions measured in cores of matrix plagioclase we 501 interpret as composition attained during recrystallization of the original aggregates during 502 burial (see also Chopin et al. 2012), part of these compositions, mainly at rims may reflect 503 also the last reequilibration of rocks on decompression. Combination of the textural argument 504 for melt presence with the very low anorthite content of plagioclase suggests crossing of the 505 H₂O-undersaturated solidus and beginning of partial melting at ~16 kbar. The calculated 506 isopleths of melt mode suggest a very small melt production around 1 mol. % (Fig. 13e). This 507 calculated volume of melt suggests that the melt was isolated in melt films, pools or pockets, 508 compatible with the observed microstructure (see Fig. 5b). Even if along this P-T path the 509 calculated molar proportion of melt increases for the whole rock, in individual textural 510 positions, as are the like-like grain boundaries, the phases may crystallize from melt in order 511 to lower the surface energy of the monomineral aggregates (e.g. Lexa et al. 2006; Hasalová et 512 al. 2008a). Likely mechanism for crystallization of albite and other phases from melt, while 513 the melt content of the rock increases, is also a process of dissolution-precipitation of these 514 phases promoted by the presence of melt and possibly also by crystallization from melt 515 (Sawyer, 2001; Hasalová et al. 2008b; Holness and Sawyer, 2008; Závada et al. 2018, Štípská 516 et al. 2019). The observed mineral assemblage q-pl-ksp-g-bi-wm-ilm with supposed former 517 melt in all rock types together with rim compositions of garnet (alm_{65-70} ; grs_{5-10} ; sps_{20-25} ; Fig. 518 9) and white mica (Si = 3.10 p.f.u.; Fig. 7a) point to last partial equilibration in the middle-P 519 part of the q-pl-ksp-g-bi-wm-ilm-liq stability field, at ~6 kbar and ~640 °C (ellipse 2 in Fig. 520 13a). Therefore, the absence of rutile and the core-to-rim zoning trends of garnet and white 521 mica in the nebulitic orthogneiss suggest a P-T path from ~14–16 kbar and ~600–740 °C to 522 ~6 kbar and ~640 °C, with local equilibration down to the ilmenite stability field and close to 523 the solidus.

Additionally, the core composition of garnet in samples of banded type II and schlieren orthogneiss is also partially to completely re-equilibrated at ~6 kbar and ~640 °C (see Fig. 9a– c), suggesting that the mineral assemblage of these rocks were melt-bearing close to the solidus.

528 *P*-*X*_{added melt} pseudosection for discussion of open-system melt infiltration

529 Previously calculated diagrams and experiments for granitic rocks in the OSD and other parts 530 of the Bohemian Massif show that depending on the exact P-T path, the rocks may produce 531 up to 7–20% of melt on decompression from peak P-T conditions of ~25 kbar (for OSD: 532 Walczak et al. 2017, for other occurrences in the Bohemian Massif: Hasalová et al. 2008c; 533 Lexa et al. 2011; Nahodilová et al. 2014). At such melt proportions, melt can be lost from the 534 rocks undergoing melting deeper in the crust, and can be added to the rocks above (Stípská et 535 al. 2019). Therefore, the effect of a possible melt gain in the studied rocks was explored in P-536 $X_{\text{added melt}}$ diagram (Fig. 14). In the calculations, the composition of the melt is taken at 16 kbar 537 and 730 °C (see black star in Fig. 13a). The $P-X_{added melt}$ diagram was calculated for the 538 whole-rock composition of the nebulitic orthogneiss at conditions of the estimated peak 539 metamorphism (T = 700 °C), and for a range of compositions between the H₂O-undersaturated 540 whole-rock composition ($X_{added melt} = 0$) and the composition with 20 mol. % of melt added 541 $(X_{\text{added melt}} = 1; \text{Fig. 14})$. The main characteristics of the diagram show a liquid-in line heading 542 from ~12 kbar for $X_{added melt} = 0$ to ~20 kbar for $X_{added melt} = 0.25$. The stability of biotite, rutile 543 and ilmenite depends on pressure in the melt-present fields and on both pressure and $X_{added melt}$ 544 in the melt-absent fields. The compositional isopleths of garnet and Si-in-phengite are 545 pressure sensitive in the melt-present fields, and do not depend on the amount of melt added 546 (Fig. 14). The horizontal arrow illustrates the effect of addition of melt to a rock with original 547 H₂O content inferred for the protolith (Fig. 13a). The starting position at $X_{added melt} = 0.05$, 548 allows the stability of the observed mineral assemblage q-pl-ksp-g-bi-wm, calculated is also 549 stability of infinitesimal amount (around 0.13-0.15 mol. %) of rutile which is not observed in 550 the rocks. The reason for this difference in the calculated and observed assemblage with 551 respect to rutile may be reequilibration on decompression to the ilmenite stability or also the 552 fact that Ti is not included in the model of white mica.

553 At $X_{\text{added melt}} = 0.09$ where the arrow crosses the solidus, the first melt appears and from 554 this point along the horizontal arrow melt proportion increases while the high grossular 555 content in garnet and high Si content in micas do not change. The position of any rock along 556 the horizontal arrow depends on the amount of melt added. The vertical part of the arrows 557 labelled A, B and C represents examples of what happens during decompression. Along the 558 arrows A, B and C the modelled mineral assemblage evolves from q-pl-ksp-g-bi-wm-ru-liq, 559 through q-pl-ksp-g-bi-wm-ru-ilm-liq to q-pl-ksp-g-bi-wm-ilm-liq until ~6.5 kbar where 560 sillimanite starts to be stable. Along the paths A, B and C the major difference is the amount 561 of melt present on decompression being at 7 kbar for A ~2 mol. % melt, B ~8 mol. % melt 562 and C ~ 22 mol. % melt. As the compositional isopleths are not dependent on the amount of 563 melt added, all the rocks evolve with identical mineral composition of garnet, white mica and 564 biotite. As the melt migration occurs, the amount of melt may increase or decrease depending 565 whether the melt is added or lost at any particular P-T conditions on decompression. The ⁵⁶⁶ rock plus melt on decompression may therefore lie anywhere from the solidus to the higher ⁵⁶⁷ values of $X_{added melt}$ of the diagram.

568 For the studied rock types, the observed assemblage q-pl-ksp-g-bi-wm-ilm, absence of 569 rutile and the core-to-rim zoning trends of garnet ($alm_{60\rightarrow70}$; $gr_{34\rightarrow5}$, $sp_{4\rightarrow22}$; Fig. 9d) and 570 white mica (Si = 3.40-3.10 p.f.u.; Fig. 7a) are compatible with a decompression path from 571 ~16 kbar to ilmenite-bearing stability field at \sim 8–13 kbar. The garnet and white mica 572 compositional isopleths are not sensitive to the amount of melt added; therefore, the melt 573 amount that percolated in individual rock types is unknown. However, consequence of 574 different melt amount in different samples may be the difference in re-equilibration along the 575 decompression path. We suggest that for the nebulitic orthogneiss that preserves HP garnet 576 core the amount of melt was low at lower pressure, thus precluding complete garnet 577 reequilibration on decompression. Re-equilibration of garnet core close to the solidus 578 observed in the banded type II and schlieren orthogneiss may be caused by higher proportion 579 of melt at lower pressure compared to the nebulitic orthogneiss. Therefore, a new P-T580 diagram with ~3.40 mol. % of re-integrated melt in the whole-composition was calculated for 581 explaining better the observed mineral assemblage and mineral compositions of the banded 582 type II and schlieren orthogneiss (Fig. 15).

⁵⁸³ *P*–*T* pseudosection with added melt

The resulting whole-rock composition after the re-integration of 3.40 mol. % melt is presented in mole percent normalized to 100% (Fig. 15a). The major features and topology of the diagram involve a displacement of the H₂O-undersaturated solidus to higher pressure, whereas the other features and topology are similar to the H₂O-undersaturated diagram (see Fig. 13).

The resulting *P*–*T* diagram shows a stability field of q-pl-ksp-g-bi-wm-ilm-liq between $\sim 4-13$ kbar and $\sim 610-740$ °C, corresponding to the observed assemblage. The *P*–*T* peak 591 conditions are defined by the high grossular content measured in garnet cores (alm_{60-65} ; grs_{30-} 592 34; sps4; Figs. 9d and 15b) preserved in nebulitic orthogneiss and the high Si content in 593 phengite cores measured in all the rock types (Si = 3.35-3.40 p.f.u.; Figs. 7a and 15c). The 594 measured albite content of plagioclase films and interstitial grains is consistent with the 595 calculated isopleth of albite at these P-T peak conditions (an_{0.05-0.02}; Fig. 15d). The last 596 equilibration at $\sim 630-640$ °C and ~ 6 kbar is constrained by the re-equilibrated compositions 597 of garnet (alm_{65-70} ; grs_{5-10} ; sps_{20-25} ; Fig. 15b) and white mica (Si = 3.10 p.f.u.; Fig. 15c). The 598 calculated isopleths of melt mode suggest a melt production during retrograde path of the 599 order of 1 mol. % resulting in up to 4 mol. % for 3.40 mol. % melt added (Fig. 15e). 600 Therefore, the mineral chemistry together with the absence of rutile record a decompression 601 path from ~15-16 kbar and ~650-740 °C to ~6 kbar and ~640 °C, with local equilibration 602 down to the ilmenite stability field and close to the solidus with the presence of melt. This 603 decompression path is compatible with the one previously described in the H₂O-604 undersaturated diagram (Fig. 13), and differs only in the melt amount present during the peak 605 and retrograde evolution, suggesting that higher melt amount may result in more profound re-606 equilibration of the assemblage close to the solidus. The melt might have been added to rocks, 607 explaining the textures, e.g. disintegration of the monomineral banding or more profound re-608 equilibration of garnet composition, but the rocks may also undergo variable degree of melt 609 loss on decompression before last cooling through the solidus.

610 **DIS**

DISCUSSION AND CONCLUSIONS

The core of the Orlica-Śnieżnik Dome (Fig. 1b) consists of two antiforms affected by various degrees of migmatization related to their distance from the site of presumed continental subduction further west (see Fig. 13 in Chopin et al. 2012a). The proximal and small Międzygórze antiform (~1 km across and ~4 km long; Fig. 1c) is characterized by heterogeneously developed zones of partial melting surrounding blocks of well-preserved H*P* 616 rocks. The distal large-scale Králíky-Śnieżnik antiform (~6–8 km across and ~20 km long; 617 Fig. 1c) was affected by widespread melting and almost complete re-equilibration of HP 618 mineral assemblages. In this work the orthogneiss of the Králíky-Śnieżnik antiform are 619 compared with those of the Międzygórze antiform in order to understand the role of melt-620 deformation interplays during the exhumation of large portions of continental crust in 621 Variscan continental collision zone.

Microstructural and geochemical arguments for grain-scale melt percolation during D2 deformation

In the study area, relics of shallow-dipping S1 foliation are folded by upright F2 folds and transposed by almost pervasive N-S trending subvertical S2 foliation (Fig. 3). This structural succession is the same as in the Międzygórze antiform but the degree of fabric transposition to subvertical fabric is significantly broader. It reaches the width of \sim 6–8 km and length of \sim 20 km, thereby attesting to a large-scale orogenic process.

A well-preserved and continuous transition from banded type II to schlieren and nebulitic orthogneiss (Fig. 4) is documented on a representative outcrop section in the central part of the Králíky-Śnieżnik antiform (Fig. 1c). The continuous transition from banded II to schlieren and nebulitic orthogneiss is commonly gradational and perpendicular to subvertical S2 transposition (Fig. 3). Therefore, by analogy to the Międzygórze antiform the studied sequence of rocks can be interpreted to reflect the higher intensity of D2 deformation.

Furthermore, the q-pl-ksp-g-bi-wm-ilm assemblage observed in all orthogneiss types is the same despite variations in meso- and micro-scale structural and textural features (see Figs. 3 and 4). The presence of cuspate K-feldspar in plagioclase layers, quartz and albite-rich plagioclase intergrowths in K-feldspar aggregates, amoeboid grains of K-feldspar in quartz layers and diffuse boundaries between different felsic layers are interpreted as a result of grain-scale melt percolation through the solid felsic rock (Figs. 4 and 5). This interpretation is

641 in agreement with previously reported examples of Hasalová et al. (2008b), Závada et al. 642 (2007, 2018) and Štípská et al. (2019) where grain boundaries were open at the micron scale 643 to fluid/melt circulation (e.g. Oliot et al. 2014). Such interpretation is also supported by slight 644 differences in chemical composition. For instance, mass balance calculations of incompatible 645 elements show the depletion of U, Zr and Hf compatible with partial dissolution of zircon in 646 the melt, implying that some melt must have been lost or must have percolated through the 647 banded type II and schlieren orthogneiss, and the gain in Ba, Sr, Eu, K and Rb corresponding 648 to a heterogeneous nucleation of interstitial feldspar from percolated melt (Fig. 11a-b). On 649 the other hand, in the nebulitic orthogneiss, mass balance calculations show the depletion of 650 Th, Cs, Pr, La, U and Ta compatible with partial dissolution of monazite in the melt, implying 651 that some melt must have been lost (Fig. 11c). Therefore, the observed textural trend from 652 banded type II to nebulitic orthogneiss can be considered not only as a result of a deformation 653 gradient but also as a result of different degree of melt infiltration/percolation of granitic 654 sources under open-system conditions (e.g. Hasalová et al. 2008; Goncalves et al. 2012; 655 Závada et al. 2018).

656 *P*–*T* evolution and melt transfer

657 The P-T path deduced from the forward-modelling indicates that the orthogneiss underwent a 658 decompression from P-T peak conditions of ~15-16 kbar and ~650-740 °C to ~6 kbar and 659 ~640 °C under the presence of melt (Figs. 13 and 15). The estimated P-T peak conditions are 660 recorded by the presence of Ca-rich garnet cores in the nebulitic orthogneiss and composition 661 of phengite in all the rock types. Subsequent decompression to ~6 kbar is recorded by the 662 core-to-rim zoning trends of garnet and white mica and absence of rutile. Similar P-T663 evolutions have been repeatedly reported from other rock types such as eclogite or HP 664 granulite occurring in the orthogneiss (~18-30 kbar and ~700-1000 °C; e.g. Pouba et al. 665 1985; Bakun-Czubarow, 1991, 1992; Steltenpohl et al. 1993; Bröcker and Klemd, 1996;

666 Kryza et al. 1996; Klemd and Bröcker, 1999; Bröcker et al. 2010; Štípská et al. 2012; Ferrero 667 et al. 2015; Budzyń et al. 2015; Jedlička et al. 2017; Walczak et al. 2017; Majka et al. 2019) 668 with retrograde paths ranging from ~9 kbar/~730 °C to ~6 kbar/~560 °C (Steltenpohl et al. 669 1993; Bröcker and Klemd, 1996; Štípská et al. 2004, 2012). Recently, prograde HP 670 metamorphism was attributed to the S1 fabric in the granitic orthogneiss close to the eclogite 671 in the Międzygórze antiform (~13-18 kbar/~700-800 °C; e.g. Chopin et al. 2012b). It was 672 also shown that migmatization of orthogneiss surrounding the Międzygórze eclogite started in 673 eclogite-facies conditions at ~15–17 kbar in the S1 fabric ($\check{S}tipska$ et al. 2019). These authors 674 also suggested that decompression along the S2 fabric from ~15-17 kbar to ~7-10 675 kbar/~690–740 °C was locally associated with anatexis. In analogy, we argue that the P-T-d676 path for the S2 vertical fabric is comparable in both antiforms (Fig. 16).

677 The modelling showed that the orthogneiss protolith from the Králíky-Śnieżnik antiform 678 is able to produce only ~1 mol. % of melt along the P-T path. However, the macro- and 679 microstructural features are typical for advanced migmatization and attest to melt presence 680 along grain boundaries (Figs. 4 and 5), suggesting that a higher melt proportion was present. 681 This is possible to achieve only if H₂O is added to the rocks, but being above the conditions 682 of the wet solidus, the hydrating fluid must have been external melt (Štípská et al. 2019). 683 Such melt is supposed to be released by similar rocks buried deeper and this is simulated in 684 the modelling by adding granitic melt to the whole-rock composition. The modelling did not 685 allow estimation of the melt proportion in the rocks based on the mineral chemical 686 composition, as the mineral chemical composition for the observed assemblage is independent 687 on the amount of melt added (Fig. 14). However, it is supposed, that rocks that contain garnet 688 with high grossular content characteristic for HP conditions contained on decompression less 689 melt compared with rocks that show garnet with re-equilibrated grossular content (see Figs. 690 13-15).

691 The melt proportion remains unknown, and may have varied along the P-T path. Melt 692 percolation started already at ~15-16 kbar and ~650-740 °C as indicated by albitic 693 composition of plagioclase in myrmekite and in interstitial films, then melt equilibrated with 694 the minerals (at least with their rim compositions) during the retrograde history to ~ 6 kbar and 695 ~640 °C. However, the amount of melt percolated is not likely to be sufficient to produce a 696 melt-supported structure required for diatexite formation (Brown, 2007; Hasalová et al. 697 2008a,b,c), but may be sufficient to allow melt-assisted granular flow (Rosenberg and Handy, 698 2005; Závada et al. 2007; Schulmann et al. 2008). This is supported by the results of Štípská 699 et al. (2019) from the Międzygórze antiform, where it was shown that different migmatite 700 textures originated from variable degree of melt-rock interaction starting at ~17 kbar and 701 ~730 °C and ending at ~7–10 kbar.

702 **Back-stop extrusion of partially molten crust**

703 Grain-scale melt percolation started locally in the S1 structure as demonstrated in the 704 Międzygórze antiform (Chopin et al. 2012b), and continued in the subvertical S2 foliation 705 where the grain-scale percolation of melt occurred along heterogeneously developed 706 subvertical narrow zones of intense D2 deformation (Fig. 16a; Štípská et al. 2019). Within 707 these subvertical zones occur low-strain domains, where the rocks preserve the shallow-708 dipping S1 fabric and high pressure conditions of 17-20 kbar. These zones of S1 foliation 709 preserve a strain gradient from banded to narrow zones of fine-grained mylonitic/migmatitic 710 orthogneiss. Across this deformation gradient the rocks show slight depletion of REE and 711 HFSE (Chopin et al. 2012b), that was explained by presence of melt in the 712 mylonitic/migmatitic orthogneiss. Because the proportion of fine-grained S1 mylonites is 713 subordinate, the proportion of melt-bearing rocks during the D1 is also subordinate. There is 714 not a geochemical study of REE and HFSE across a strain gradient related to the S2 fabric in 715 the Miedzygórze antiform. However, as the proportion of schlieren and nebulitic orthogneiss types is higher in the S2 compared to S1 we extrapolate the depletion of REE and HFSE also
to the S2 migmatitic fabric (Fig. 16a).

718 In the Králíky-Śnieżnik antiform the D2 deformation affects almost homogenously the 719 whole volume of the felsic orthogneiss with only rare relics of low-strain S1 domains (Fig. 720 16b). The degree of transposition of S1 by S2, together with high proportion of schlieren and 721 nebulitic orthogneiss types in S2 fabric implies also that melt percolation affected 722 significantly larger proportion of crust during D2 compared to the Miedzygórze antiform. The 723 orthogneiss samples from this study, from a large zone of almost homogeneous D2 724 deformation show similar degree of REE and HFSE depletion (Fig. 10c) as the mylonitic type 725 of Chopin et al. (2012b) from the Międzygórze antiform, which was interpreted as a result of 726 presence of melt during deformation. Because the zone of D2 deformation and proportion of 727 the migmatitic types is significantly higher in the Králíky-Śnieżnik antiform, the total 728 depletion REE and HFSE in this portion of crust is much more important compared to the 729 Międzygórze antiform (Fig. 16b). Another important feature is the last reequilibration of 730 rocks marked by mineral rim chemistry, under the presence of melt, along the decompression 731 P-T path. The rocks from the Międzygórze antiform show last reequilibration under the 732 presence of melt at ~10 kbar while the rocks from the Králíky-Śnieżnik antiform show 733 reequilibration under the presence of melt at ~ 5 kbar. This implies that the difference in total 734 exhumation between two antiforms under the presence of melt within the D2 zone is 735 significantly higher in the case of the Králíky-Śnieżnik antiform compared to the 736 Międzygórze antiform.

Based on our petrological data it may be concluded that melt percolation along vertical D2
deformation zone facilitated exhumation of HP rocks in core of the two antiforms from ~60
km to 35 km (Międzygórze antiform, Fig, 16a) and ~50 km to >20 km (Králíky-Śnieżnik
antiform, Fig. 16b), allowing the juxtaposition of originally HP orthogneiss with MP rocks in

crustal-scale synforms (see also Štípská et al. 2004; Chopin et al. 2012a; Štípská et al. 2012,
2019). Another point that reinforces the role of the presence of melt for facilitating extrusion
of these deep rocks is a fact that the presence even of small melt volumes plays a major role
in decreasing the strength of the rocks (Rosenberg and Handy, 2005).

745 The above described deformation was related to horizontal shortening of collisional 746 wedge that contributed to the vertical extrusion of partially molten crust en masse in the 747 eastern part of the OSD. Such an extrusion of weak material is pronounced in particular close 748 to the Brunia back-stop where massive portions of rheologically weak and partially molten 749 rocks flowed upwards under horizontal stress from the root area of the orogenic wedge (Fig. 750 16). The extrusion model proposed by Thompson et al. (1997a,b) is suitable to well explain 751 the exceptionally high rate of exhumation suggested already by Steltenpohl et al. (1993) and 752 the shape of P-T path depicted by this study. Majka et al. (2019) suggested that first part of 753 exhumation occurred in channel flow region of the subducted continental margin along the 754 rigid buttress of the Brunovistulian microcontinent and that folding of the entire crustal 755 sequence occurred in the shallower part of the accretionary wedge. The minimum depth for 756 the F2 folding from this study and from *Štípská* et al. (2019) is ~16–17 kbar. Recently, the 757 numerical modelling of Maierová et al. (2014) tested various parameters controlling the 758 exhumation rates of hot gneiss domes and corresponding P-T-t paths such as rate of 759 convergence, heat production and erosion. These authors concluded that in the case of the 760 Orlica-Śnieżnik Dome the gravitational instability contribution was minor compared to 761 laterally forced folding leading to gneiss dome formation and exhumation of hot felsic lower 762 crust. All the above mentioned models tacitly suppose extreme weakness of thermally 763 softened hot felsic lower crust allowing homogeneous vertical flow. However, in detail, both 764 meso- and micro-scale mechanism allowing the extreme drop of strength of the felsic crust 765 remain enigmatic. Only recently, natural observations from hot gneiss domes and their analogue modelling suggest that partial melting can trigger detachment folding and vertical flow of migmatites and granitoids (Lehmann et al. 2017). Based on our study we argue that the grain-scale melt percolation (called also reactive porous flow, melt infiltration) represents such a principal weakening mechanism allowing homogeneous flow of crust typical for extrusion. It is probably also a principal mechanism controlling exhumation of deep partially molten crust in hot collisional orogens such as the European Variscan belt.

772 ACKNOWLEDGMENTS

This work was financially supported by the Czech national grant agency (GAČR 16-17457s
and 19-25035s to P. Štípská). We would like to thank E. Oliot from Montpellier University
for his useful discussions about fluids-rocks interactions during the course of this work. We
are also grateful to M. Racek from Charles University for operating the SEM and EPMA.
Detailed constructive comments provided by J. Szczepański and R. Weinberg, editor in chief
Wolf-Christian Dullo and guest editor P. Jeřábek are greatly appreciated.

779 **REFERENCES**

Aleksandrowski P, Kryza R, Mazur S, Żaba J (1997) Kinematic data on major Variscan
strike-slip fault and shear zones in the Polish Sudetes, northeast Bohemian Massif.
Geological Magazine 134(5): 727–739.

Aleksandrowski P, Mazur S (2002) Collage tectonics in the norhteasternmost part of the
Variscan Belt: the Sudetes, Bohemian Massif. In: Winchester JA, Pharaoh TC, Vernier J,
(eds) Palaeozoic Amalgation of Central Europe: Geological Society of London Special
Publications 201, pp 237–277.

Anczkiewicz R, Szczepański J, Mazur S, Storey C, Crowley Q, Villa IM, Thrilwall ME,
Jeffries TE (2007) Lu–Hf geochronology and trace element distribution in garnet:

- 789 Implications for uplift and exhumation of ultra-high pressure granulites in the Sudetes,
 790 SW Poland. Lithos 95(3-4): 363–380.
- Bakun-Czubarow N (1991) On the possibility of occurrence of quartz pseudomorph after
 coesite in the eclogite-granulite rock series of the Złote Mountains in the Sudetes (SW
 Poland). Archive Mineral 47(1): 5–16.
- Bakun-Czubarow N (1992) Quartz pseudomorphs after coesite and quartz exsolutions in
 eclogitic omphacites of the Złote Mountains in the Sudetes (SW Poland). Archiwum
 Mineralogiczne 48(1-2): 3–25.
- Barker DS (1970) Composition of granophyre, myrmekite, and graphic granite. Geological
 Society of America Bullettin 81: 3339–3350.
- Białek D, Werner T (2004) Geochemistry and geochronology of the Javornik granodiorite and
 its geodynamic significance in the Eastern Variscan Belt. Geolines 17: 22–23.
- Borkowska M, Dörr W (1998) Some remarks on the age and mineral chemistry of orthogneiss
 from the Ladek-Śnieżnik Metamorphic Massif Sudetes, Poland. Terra Nostra 98(2): 27–
 30.
- Bröcker M, Klemd R (1996) Ultrahigh-pressure metamorphism in the Śnieżnik Mountains
 (Sudetes, Poland): P-T constraints and geological implications. Journal of Geology
 104(4): 417–433.
- Bröcker M, Klemd R, Cosca M, Brock W, Larionov AN, Rodionov N (2009) The timing of
 eclogite facies metamorphism and migmatization in the Orlica-Śnieżnik complex,
 Bohemian Massif: Constraints from a multimethod geochronological study. Journal of
 Metamorphic Geology 27(5): 385–403.
- 811 Bröcker M, Klemd R, Kooijman E, Berndt J, Larionov A (2010) Zircon geochronology and
- trace element characteristics of eclogites and granulites from the Orlica-Śnieżnik complex,
- 813 Bohemian Massif. Geological Magazine 147(3): 339–362.

- Brown M, Solar GS (1998) Shear-zone and melts: feedback relations and self-organization in
 orogenic belts. Journal of Structural Geology 20(2-3): 211–227.
- Brown M (2007) Metamorphic conditions in orogenic belts: A record of secular change.
 International Geology Review 49(3): 193–234.
- Budzyń B, Jastrzębski M, Kozub-Budzyń G, Konečyń P (2015) Monazite Th–Utotal–Pb
 geochronology and *P*–*T* thermodynamic modelling in a revision of the H*P*–H*T*metamorphic record in granulites from Stary Gierałtów (NE Orlica-Śnieżnik Dome, SW
 Poland). Geological Quarterly 59: 700–717.
- Chopin F, Schulmann K, Skrzypek E, Lexa O, Martelat JE, Lehmann J, Corsini M, Dujardin
 JR, Edel JB, Štípská P, Pitra P (2012a) Crustal influx, indentation, ductile thinning and
 gravity redistribution in a continental wedge: building a Moldanubian mantled gneiss
 dome with underthrust Saxothuringian material (European Variscan belt). Tectonics
 31(TC1013): 1–27.
- Chopin F, Schulmann K, Štípská P, Martelat, JE, Pitra P, Lexa O, Petri B (2012b)
 Microstructural and metamorphic evolution of a high pressure granitic orthogneiss during
 continental subduction (Orlica-Śnieżnik dome, Bohemian Massif). Journal of
 Metamorphic Geology 30: 347–376. doi:10.1111/j.1525-1314.2011.00970.x
- Collins WJ, Sawyer EW (1996) Pervasive granitoid magma transfer through the lower-middle
 crust during non-coaxial compressional deformation. Journal of Metamorphic Geology
 14: 565–579.
- Coggon R, Holland TJB (2002). Mixing properties of phengitic micas and revised garnetphengite thermobarometers. Journal of Metamorphic Geology 20: 683–696.
- Base Don J (1964) Góry Złote i Krowiarki jako elementy składowe metamorfiku Śnieżnik (The
 Złote and Krowiarki Mountians as structural elements of the Śnieżnik metamorphic
- 838 massif). Geologia Sudetica 1: 79–117.

- B39 Don J (1982) The Sienna synform and the relationship of gneisses to the deformational stages
 distinguished in the Śnieżnik metamorphic massif (Sudetes). Geologia Sudetica 17:
 130–124.
- Don J, Dumick M, Wojciechowska I, Żelaźmiewicz A (1990) Lithology and tectonics of the
 Orlica-Śnieżniek Dome, Sudetes Recent state of knowledge. Neues Jahrbuch für
 Geologie und Paläeontologie Abhandlungen. 179(2-3): 159–188.
- B45 Don J, Skácel J, Gotowała R (2003) The boundary zone of the East and West Sudetes on the
 1:50000 scale geological map of the Velké Vrbno, Staré Město and Śnieżnik
 Metamorphic Units. Geologia Sudetica 35(1): 25–59.
- 848 Eskola P.E. (1948). The problems of mantles gneiss domes. Quarterly Journal of the
 849 Geological Society 104: 461–476.
- Evensen NM, Hamilton PJ, O'Nions RK (1978) Rare-earth abundances in chondritic
 meteorites. Geochimica et Cosmochimica Acta 42: 1199–1212.
- Ferrero S, Wunder B, Walczak K, O'Brien PJ, Ziemann MA (2015) Preserved near ultrahighpressure melt from continental crust subducted to mantle depths. Geology 43: 447–450.
- Fischer G (1936) Der Bau des Glatzer Scchneegebirges, Jahrb. Preuss. Geol. Landesanst. 56:
 712–732.
- Franke W, Zelaźniewicz A (2000) The eastern termination of the Variscides: Terrane
 correlation and kinematic evolution. In: Franke W, et al. (eds) Orogenic Processes:
 Quantification and Modelling in the Variscan Belt. Geological Society Special Publication
 179: 63–86.
- 860 Goncalves Ph, Oliot E, Marquer D, Connolly JAD (2012) Role of chemical processes on
- 861 shear zone formation: an example from the Grimsel metagranodiorite (Aar massif, Central
- Alps). Journal of Metamorphic Geology 30(7): 703–722.

- Grant JA (1986) The isocon diagram-a simple solution to Gresens' equation for metasomatic
 alteration. Economic Geology 81(8): 1976–1982.
- Hasalová P, Schulmann K, Lexa O, Štípská P, Hrouda F, Ulrich S, Haloda J, Týcová P
 (2008a) Origin of migmatites by deformation-enhanced melt infiltration of orthogneiss: a
 new model based on quantitative microstructural analysis. Journal of Metamorphic
 Geology 26: 29–53.
- Hasalová P. Janoušek V, Schulmann K, Štípská P, Erban V (2008b) From orthogneiss to
 migmatite: geochemical assessment of the melt infiltration model in the Gföhl Unit
 (Moldanubian Zone, Bohemian Massif). Lithos 102: 508–537.
- Hasalová P, Štípská P, Powell R, Schulmann K, Janoušek V, Lexa O (2008c) Transforming
 mylonitic metagranite by open-system interactions during melt flow. Journal of
 Metamorphic Geology 26: 55–80.
- Holland TJB, Powell R (1998) An internally consistent thermodynamic data set for phases of
 petrological interest. Journal of Metamorphic Geology 16: 309–343.
- Holland TJB, Powell R (2003). Activity-composition relations for phases in petrological
 calculations: an asymmetric multicomponent formulation. Contributions to Mineralogy
 and Petrology 145: 492–501.
- Hollister LS (1993) The role of melt in the uplift and exhumation of orogenic belts. Chemical
 Geology 108: 31–48.
- Holness MB, Sawyer EW (2008) On the pseudomorphing of melt-filled pores during the
 crystallization of migmatites. Journal of Petrology 49: 1343–1363.
- Hopkins MB, Harrison TM, Manning CE (2010) Constraints on Hadean geodynamic from
 mineral inclusions in >4 Ga zircons. Earth and Planetary Science Letters 298: 367–376.
- 886 Jastrzębski M (2009) A Variscan continental collision of the West Sudetes and the
- 887 Brunovistulian terrane: A contribution from structural and metamorphic record of the

888 Stronie Formation, the Orlica-Śnieżnik Dome, SW Poland. International Journal of Earth
889 Sciences 98: 1901–1923.

- Jastrzębski M, Żelaźniewicz A, Nowak I, Murtezi M, Larionov AN (2010) Protolith age and
 provenance of metasedimentary rocks in Variscan allochthon units: U–Pb SHRIMP zircon
 data from the Orlica-Śnieżnik Dome, West Sudetes. Geological Magazine 147(3):
 416–433.
- Jastrzębski M, Budzyń B, Stawikowski W (2016) Structural, metamorphic and
 geochronological record in the Goszów quartzites of the Orlica-Śnieżnik Dome (SW
 Poland): implications for the polyphase Variscan tectonometamorphism of the
 Saxothuringian terrane. Geological Journal 51(3): 455–479
- Jastrzebski M, Budzyń B, Stawikowski W (2017) Cambro-Ordovician vs DevonoCarboniferous geodynamic evolution of the Bohemian Massif: evidence from P–T–t
 studies in the Orlica-Śnieżnik Dome, SW Poland. Geological Magazine 156(3): 447–470.
- Jedlička R, Faryad SW (2017) Felsic granulite with layers of eclogite facie rocks in the
 Bohemian Massif; did they share a common metamorphic history? Lithos 286-287: 408–
 425.
- Klemd R, Bröcker M, Schramm J (1995) Characterization of amphibolite-facies fluids of
 Variscan eclogites from the Orlica-Śnieżnik dome (Sudetes, SW Poland). Chemical
 Geology 119: 101–113.
- Klemd R, Bröcker M (1999) Fluid influence on mineral reactions in ultrahigh-pressure
 granulites: a case study in the Śnieżnik Mts. (West Sudetes, Poland). Contributions to
 Mineralogy and Petrology 136(4): 358–373.
- 910 Kozłowski K (1961) Kompleks granulitowy Starego Gierałtowa w Górach Złlotych (The
 911 granulitic complex of Stary Gierałtow East Sudetes). Archive of Mineralogy 25: 5–123.

- Kröner A, Štípská P, Schulmann K, Jaeckel P (2000) Chronological constraints on the preVariscan evolution of the Northeastern margin of the Bohemian Massif, Czech Republic.
 In: Franke W, et al. Orogenic Processes; Quantification and Modelling in the Variscan
 Belt. Geological Society Special Publication 179: 175–197.
- 917 isotopic systematics of early Palaeozoic granitoid gneisses from the Czech and Polish
 918 Sudetes (Jizerské hory, Krkonoše Mountains and Orlice-Śnieżnik Complex). International

Kröner A, Jaeckel P, Hegner E, Opletal M (2001) Single zircon ages and whole rock Nd

919 Journal of Earth Sciences 90: 304–324.

- 920 Kryza R, Pin C, Vielzeuf D (1996) High-pressure granulites from the Sudetes (South-west
 921 Poland): Evidence of crustal subduction and collisional thickening in the Variscan Belt.
- Journal of Metamorphic Geology 14: 531–546.
- Lange U, Bröcker M, Mezger K, Don J (2002) Geochemistry and Rb–Sr geochronology of a
 ductile shear zone in the Orlica-Śnieżnik dome (West Sudetes, Poland). International
 Journal of Earth Sciences 91(6): 1005–1016.
- Lange U, Bröcker M, Armstrong R, Zelazniewicz A, Trapp E, Mezger K (2005) The
 orthogneiss of the Orlica-Śnieżnik complex (West Sudetes, Poland): geochemical
 characteristics, the importance of pre-Variscan migmatization and constraints on the
 cooling history. Journal of the Geological Society 162: 973–984.
- Lehmann J, Schulmann K, Edel JB, Ježek J, Hrouda F, Lexa O, Chopin F (2013) Structural
 and anisotropy of magnetic susceptibility records of granitoids sheets emplacement during
 growth of a continental gneiss dome (Central Sudetes, European Variscan Belt). Tectonics
 32: 1–23.
- Lehmann J, Schulmann K, Lexa O, Závada P, Štípská P, Hasalová P, Belyanin G, Corsini M
 (2017) Detachment folding of partially molten crust in accretionary orogens: A new
 magma-enhanced vertical mass and heat transfer mechanism. Lithosphere 9(6): 889–909.

- 937 Lexa O, Štípská P, Schulmann K, Baratoux L, Kröner A (2006) Contrasting textural record of
 938 two distinct metamorphic events of similar P-T conditions and different duration. Journal
 939 of Metamorphic Petrology 23(8): 649–666.
- Lexa O, Schulmann K, Janoušek V, Štípská P, Guy A, Racek M (2011) Heat sources and
 trigger mechanisms of exhumation of HP granulites in Variscan orogenic root. Journal of
- 942 Metamorphic Geology 29: 79–102.
- 943 Lopez-Moro FJ (2012) EASYGRESGRANT A Microsoft Excel spreadsheet to quantify
 944 volume changes and to perform mass-balance modelling in metasomatic systems:
 945 Computer and Geosciences 39: 191–196.
- Maierová P, Lexa O, Schulmann K, Štípská P (2014) Contrasting tectono-metamorphic
 evolution of orogenic lower crust in the Bohemian Massif: A numerical mode. Gondwana
 Research 25(2): 509–521.
- 949 Majka J, Mazur S, Młynarska M, Klonowska I, Tual L, Kośmińska K, Tarasiuk J, Wroński S
- 950 (2019) Integrating X-ray mapping and microtomography of garnet with thermobarometry
- to define the *P*–*T* evolution of the (near) UHP Miedzygorze eclogite, Sudetes, SW Poland.
- Journal of Metamorphic Geology 37: 97–112.
- Maluski H, Rajlich P, Souček J (1995) Pre-Variscan, Variscan and early Alpine thermostectonic history of the northeastern Bohemian Massif: 40Ar/39Ar study. Geologische
 Rundschau 84: 345–358.
- Marquer D, Burkhard M (1992) Fluid circulation, progressive deformation and mass-transfer
 processes in the upper crust: the example of basement-cover relationships in the External
 Crystalline Massifs, Switzerland. Journal of Structural Geology 14(8–9): 1047–1057.
- Mazur S, Aleksandrowski P (2001) The Tepla(?)/Saxothuringian suture in the KarkonoszeIzera massif, Western Sudetes, Central European Variscides, Internacional Journal of
 - 961 Earth Sciences 90(2): 341–360.

962	Mazur S, Kröner A, Szczepański J, Turniak K, Hanžl P, Melichar R, Rodionov NV, Paderin I,
963	Sergeev SA (2010) Single zircon U-Pb ages and geochemistry of granitoid gneisses from
964	SW Poland: Evidence for an Avalonian affinity of the Brunian microcontinent. Geological
965	Magazine 174(4): 508–526.
966	Mazur S, Szczepański J, Turniak K, McNaughton N (2012) Location of the Rheic suture in
967	the eastern Bohemian Massif: Evidence from detrital zircon data. Terra Nova 24: 199-
968	206.

- 969 Mehnert KR (1971) Migmatites and the origin of granitic rocks. Elsevier, Amsterdam.
- 970 Murtezi M (2006) The acid metavolcanic rocks of the Orlica-Śnieżnik Dome (Sudete): Their

971 origin and tectono-metamorphic evolution. Geologia Sudetica 38: 1–38.

- 972 Nahodilová R, Štípská P, Powell R, Košler J, Racek M (2014) High-Ti muscovite as a
 973 prograde relict in high pressure granulites with metamorphic Devonian zircon ages
 974 (Běstvina granulite body, Bohemian Massif): Consequences for the relamination model of
 975 subducted crust. Gondwana Research 258: 630–648.
- 976 Nahodilová R, Hasalová P, Štípská P, Schulmann K, Závada P, Míková J, Kylander-Clark A,
- 977 Maierová P (2020) Exhumation of subducted continental crust along the arc region.
 978 Gondwana Research 80: 157–187.
- Oliot E, Goncalves Ph, Schulmann K, Marquer D, Lexa O (2014) Mid-crustal shear zone
 formation in granitic rocks: Contraints from quantitative textural and crystallographic
 preferred orientations analyses. Tectonophysics 612-613: 63–80.
- Oliver GJH, Corfu F, Krogh TE (1993) U–Pb ages from SW Poland: Evidence for a
 Caledonian suture zone between Baltica and Gondwana. Journal of Geology Society 150:
 355–369.
- Potdevin JL, Marquer D (1987) Quantitative methods for the estimation of mass transfers by
 fluids in deformed metamorphic rocks (Méthodes de quantification des transferts de

987 matiére par les fluids dans les roches métamorphiques déformées). Geodinamica Acta 1:
988 193–206.

Pouba Z, Paděra K, Fiala J (1985) Omphacite granulite from the NE margin of the Bohemian
Massif (Rychleby Mountains). Neus Jahrbuch für Mineralogie - Abhandlungen 151: 29–
52.

- Powell R, Holland TJB, Worley B (1998) Calculating phase diagrams involving solid
 solutions via non-linear equations, with examples using THERMOCALC. Journal of
 Metamorphic Geology 16: 577–588.
- Pressler RE, Schneider DA, Petronis MS, Holm DK, Geissman JW (2007) Pervasive
 horizontal fabric and rapid vertical extrusion: Lateral overturning and margin sub-parallel
 flow of deep crustal migmatites, northeastern Bohemian Massif. Tectonophysics 443(1-2):
 19–36.
- Rosenberg CL, Handy M (2005) Experimental deformation of partially melted granite
 revisited: Implications for the continental crust. Journal of Metamorphic Geology 23: 19–
 28.
- Sawyer EW (2001) Melt segregation in the continental crust: distribution and movement of
 melt in anatectic rocks. Journal of Metamorphic Geology 19: 291–309.
- Schneider DA, Zahniser SJ, Glascock JM, Gordon SM, Manecki M (2006)
 Thermochronology of the West Sudetes (Bohemian Massif): Rapid and repeated eduction
 in the Eastern Variscides, Polamd and Czech Republic. American Journal Science
 306(10): 846–873.
- Schulmann K, Martelat J-E, Ulrich S, Lexa O, Štípská P, Becker JK (2008) Evolution of
 microstructure and melt topology in partially molten granitic mylonite: Implications for
 rheology of felsic middle crust. Journal of Geophysical Research-Solid Earth 113(B10).

- Skrzypek E, Schulmann K, Štípská P, Chopin F, Lehmann J, Lexa O, Haloda J (2011a)
 Tectono-metamorphic history recorded in garnet porphyroblasts: Insights from
 thermodynamic modelling and electron backscatter diffraction analysis of inclusion trails.
- 1014 Journal of Metamorphic Geology 29: 473–496.
- 1015 Skrzypek E, Štípská P, Schulmann K, Lexa O, Lexová M, (2011b) Prograde and retrograde
- 1016 metamorphic fabrics a key for understanding burial and exhumation in orogens
 1017 (Bohemian Massif). Journal of Metamorphic Geology 29: 451–472.
- 1018 Skrzypek E, Lehmann J, Szczepański J, Anczkiewicz R, Štípská P, Schulmann K, Kröner A,
- 1019 Białek D (2014) Time-scale of deformation and intertectonic phases revealed by *P*–*T*–*D*–*t*
- 1020 relationships in the orogenic middle crust od the Orlica-Śnieżnik Dome, Polish/Czech
- 1021 Central Sudetes. Journal of Metamorphic Geology 32: 981–1003.
- Smulikowski K (1967) Eklogite Gór Śnieznickich w Sudetach (Eclogites of the Śnieżnik
 Mountains in the Sudetes). Geologia Sudetica 3: 157–174.
- Steltenpohl MG, Cymerman Z, Krogh EJ, Kunk MJ (1993) Exhumation of eclogitized
 continental basement collapse, Sudety Mountains, Poland. Geology 21: 1111–1114.
- 1026 Štípská P, Schulmann K, Kröner A (2004) Vertical extrusion and middle crustal spreading of
- 1027 omphacite granulite: A model of syn-convergent exhumation (Bohemian Massif, Czech
 1028 Republic). Journal of Metamorphic Geology 22(3): 179–198.
- 1029 Štípská P, Powell R (2005) Does ternary feldspar constrain the metamorphic conditions of
 1030 high-grade meta-igneous rocks? Evidence from orthopyroxene granulites, Bohemia
 1031 Massif. Journal of Metamorphic Geology 23: 627–647.
- 1032 Štípská P, Schulmann K, Powell R (2008) Contrasting metamorphic histories of lenses of
- 1033 high-pressure rocks and host migmatites with a flat orogenic fabric (Bohemian Massif,
- 1034 Czech Republic): A result of tectonic mixing within horizontal crustal flow? Journal of
- 1035 Metamorphic Geology 26: 623–646.

- 1036 Štípská P, Chopin F, Skrzypek E, Schulmann K, Lexa O, Pitra P, Martelat J-E, Bolinger C,
- 1037 Žáčková E (2012) The juxtaposition of eclogite and mid-crustal rocks in the Orlica-
- 1038 Śnieżnik Dome, Bohemian Massif. Journal of Metamorphic Geology 30(2): 231–234.
- 1039 doi:10.1111/j.1525-1314.2011.00964.x.
- 1040 Štípská P, Hasalová P, Powell R, Závada P, Schulmann K, Racek M, Aguilar C, Chopin F
- 1041 (2019) The effect of melt infiltration on metagranitic rocks: The Śnieżnik Dome,
 1042 Bohemian Massif. Journal of Petrology 60: 591–618.
- Stuart CA, Piazolo S, Daczko NR (2018) The recognition of former melt flux through highstrain zones. Journal of Metamorphic Geology 00: 1–21.
- Thompson AB, Schulmann K, Jezek J (1997a) Extrusion tectonics and elevation of lower
 crustal metamorphic rocks in convergent orogens. Geology 25(6): 491–496.
- 1047 Thompson AB, Schulmann K, Jezek J (1997b) Thermal evolution and exhumation in
 1048 obliquely convergent (transpressive) orogens. Tectonophysics 280: 171–184.
- Turniak K, Mazur S, Wysoczański R (2000) SHRIMP zircon geochronology and
 geochemistry of the Orlica-Śnieżnik gneisses (Variscan belt of Central Europe) and their
 tectonic implications. Geodinamia Acta 13: 293–312.
- 1052 Walczak K, Anczkiewicz R, Szczepański J, Rubatto D, Košler J (2017) Combined garnet and
- 1053 zircon geochronology of the ultra-high temperature metamorphism: Constraints on the rise
- 1054 of the Orlica-Śnieżnik Dome, NE Bohemian Massif, SW Poland. Lithos 292-293: 388–
- 1055 400. https://doi.org/10.1016/j.lithos.2017.09.013
- 1056 Vanderhaeghe O (2001) Melt segregation, pervasive melt migration and magma mobility in
- the continental crust: The structural record from pores to orogens. Physic and Chemistry
 of the Earth (A) 26(4-5): 213–223.
- 1059 Vangerow EF (1943) Das Normalprofil des Algonkium und Kambriums in den mittleren
- 1060 Sudeten. Geologische Rundschau 34: 10–12.

- Weinberg RF (1999) Mesoscale pervasive felsic magma migration: alternative to dyking.
 Lithos 46: 393–410.
- White RW, Pomroy E, Powell R (2005) An in situ metatexite-diatexite transition in upper
 amphibolite facies rocks from Broken Hill, Australia. Journal of Metamorphic Geology
 23: 579–602.
- White RW, Powell R, Holland TJB (2007) Progress relating to calculation of partial melting
 equilibria for metapelites. Journal of Metamorphic Geology 25: 511–527.
- Young DJ, Kylander-Clark ARC (2015) Does continental crust transform during eclogite
 facies metamorphism? Journal of Metamorphic Geology 33: 331–357.
- 1070 Závada P, Schulmann K, Konopasek J, Ulrich S, Lexa O (2007) Extreme ductility of feldspar
 1071 aggregates Melt-enhanced grain boundary sliding and creep failure: Rheological
 1072 implications for felsic lower crust. Journal of Geophysical Research-Solid Earth 112.
- 1073 Závada P, Schulmann K, Racek M, Hasalová P, Jeřábek P, Weinberg RF, Štípská P, Roberts
- 1074 Al (2018) Role of strain localization and melt flow on exhumation of deeply subducted 1075 continental crus. Lithosphere 10(2): 217–238.
- 1076 Żelaźniewicz A, Mazur S, Szczepański J (2002) The Ladek-Śnieżnik Metamorphic Unit1077 Recent state of Knowledge. Geolines 14: 115–125.
- Żelaźniewicz A, Nowak I, Larionov A, Presnyakov S (2006) Syntectonic Lower Ordovician
 migmatite and post-tectonic Upper Viséan syenite in the Western limb of the OrlicaŚnieżnik Dome, West Sudetes: U–Pb SHRIMP data from zircons. Geologia Sudetica, 38:
 63–80.

1082 FIGURE AND TABLE CAPTIONS

Fig. 01. (a) Lithotectonic map of North European Variscan belt (modified after
Aleksandrowski et al. 1997; Don et al. 2003, Żelaźniewicz et al. 2006). The position of
Orlica-Śnieżnik Dome is outlined. (b) Geological sketch map of the Orlica-Śnieżnik Dome

(modified after Aleksandrowski et al. 1997; Don et al. 2003; Żelaźniewicz et al. 2006). (c)
Geological and structural map of Międzygórze and Králíky-Śnieżnik antiforms (lithologies after Don et al. 2003; Chopin et al. 2012a,b; Štípská et al. 2012). The location of the orthogneiss used in this study and the position of the structural profiles are indicated.

Fig. 02. Interpretative cross-sections showing the main structural relationships between both
 antiforms (a–b) and the different orthogneiss types. See Figure 1c for locations of profiles.

Fig. 03. (a) Outcrop photograph illustrating a lithological sketch (see legend in the Figures 1
and 2) and the locations of studied samples with white stars. (b–f) Field photographs showing
the different textural rocks displayed, ranging from banded type II to schlieren and nebulitic
orthogneiss.

1096 Fig. 04. Representative CL image mosaics showing textural features of the different rock 1097 types: (a) banded type II orthogneiss (sample FC076B): alternation of individual layers of 1098 recrystallized K-feldspar, quartz and plagioclase distinctly defined, with less diffuse 1099 boundaries between individual layers. (b) Banded type II orthogneiss (samples FC076E): 1100 alternation of almost individual layers of recrystallized K-feldspar, quartz and plagioclase 1101 with highly diffuse boundary between feldspar layers. (c) Schlieren orthogneiss (sample 1102 FC076J) characterised by relics of K-felsdpar-rich layers in otherwise isotropic matrix. (d) 1103 Nebulitic orthogneiss (samples FC076C) with no relics of original banding.

Fig. 05. Detailed back scattered electron (BSE) and cathodoluminescence (CL) images of different rock types. (a) Diffuse boundary between a layers of mixed aggregates and a Kfeldspar-rich layer with numerous interstitial plagioclase, quartz and myrmekite. (b) Detail of cuspate plagioclase, rounded quartz and myrmekite as interstitial phases in K-feldspar layer. (c) Quartz- and plagioclase-rich layers with interstitial grains of feldspar and quartz. Phengite is surrounded by biotite and biotite occurs also along cleavage of phengite. (d) Large crystal of plagioclase with and antiperthitic core rich in exsolutions of K-feldspar. (e) Garnet in a matrix of quartz, plagioclase, K-feldspar, phengite, biotite and myrmekite. (f) Symplectite of
quartz and white mica at the boundary of K-feldspar and phengite. (g) Large phengite laths
with biotite at margins and along the cleavage.

1114 **Fig. 06.** Composition of feldspar (an = (Ca/(Ca+Na+K))*100 in blue color and or = 1115 (K/(Ca+Na+K))*100 in yellow color) for the different rock types localized in different 1116 microstructural positions (a-f). Representative analyses are listed in Table 1.

- Fig. 07. Composition of white mica: (a) Si (p.f.u.) content of white micas *v*. samples. Note the decrease in Si (p.f.u.) content from cores to rim. (b–c) Compositional ranges from cores to rims of white micas. Grey and yellow arrows indicate zoning from core to rim. Representative analyses are listed in Table 2.
- Fig. 08. Composition of biotite for the different rock types (a, b). Representative analyses arelisted in Table 2.
- Fig. 09. Garnet compositional trends of the different rock types: (a) weakly migmatized
 banded type II orthogneiss (sample FC076B); (b) banded type II orthogneiss (sample
 FC076E); (c) schlieren orthogneiss (sample FC076J): and (d) nebulitic orthogneiss (FC076C).
 Representative analyses are listed in Table 3.

1127 Fig. 10. Isocon diagrams after Grant (1986) comparing: (a) the average whole-rock 1128 composition of schlieren orthogneiss and (b) the whole-rock composition of the nebulitic 1129 orthogneiss (vertical axis) with respect to the composition of the weakly migmatized banded 1130 type II orthogneiss (sample FC076A). The diagrams (a) and (b) show loss and/or gain of 1131 major elements with respect to composition of reference rock plotted as reference line. (c) 1132 Spider plot normalized to chondrite (Evensen et al. 1978). Shaded field corresponds to the 1133 orthogneiss types described by Chopin et al. (2012b) in the Międzygórze antiform. (d) Spider 1134 plot normalized to weakly migmatized banded type II orthogneiss (sample FC076A).

1135 Fig. 11. Potdevin diagrams (Potdevin and Marquer, 1987; Lopez-Moro, 2012) illustrating the 1136 loss-gain relationships for a range of incompatible elements for banded type II, schlieren and 1137 nebulitic orthogneiss compared to weakly migmatized banded type II orthogneiss (sample 1138 FC076A). Relative gain or loss of mass (Δm_i) is normalized by the initial mass (m_i^0) in the 1139 volume-composition diagrams. The volume factor (F_v) is given by the volume ratio between 1140 the transformed rocks and initial one. Shaded area refers to the magmatic fluctuation ranges 1141 (immobile elements) and solid lines to mobile elements. LILE = Large Ion Lithophile 1142 Elements, HFSE = High Field Strength Elements, REE = Rare Earth Elements. (see Table 5).

Fig. 12. *P-M*(H₂O) pseudosection calculated at 7 kbar for a nebulitic orthogneiss (sample FC076C) and contoured for the calculated spessartine (m(sps)), almandine (x(alm)) and grossular (z(grs)) contents of garnet and for the molar proportion of liquid (liq (mol. %)). The solidus is emphasized by a dark-dashed line. Quartz, plagioclase and K-feldspar are present in all fields.

1148 Fig. 13. (a) P-T pseudosection calculated for the analysed whole-rock composition of a 1149 nebulitic orthogneiss (sample FC076C). (b-e) Simplified pseudosections with compositional 1150 isopleths of spessartine (m(sps)), almandine (x(alm)) and grossular (z(grs)) in garnet; Si 1151 content of white mica (Si(wm) p.f.u.); anorthite content of plagioclase (ca(pl)); and molar 1152 proportion of melt (liq (mol. %)). The ellipses indicate the P-T ranges compatible with the 1153 observed assemblage and core and rim compositions of garnet and white mica. The star 1154 indicates P-T conditions from which the melt composition was taken to be reintegrated into 1155 whole-rock composition shown in Figures 14 and 15. The solidus is underlined by a thick 1156 black dashed line. See text for discussion of the P-T path.

Fig. 14. $T-X_{added melt}$ pseudosection calculated at 700 °C for a range of compositions representing mixtures of H₂O-undersaturated whole-rock composition of the nebulitic orthogneiss (x = 0) and the composition of melt calculated at 680 °C and 16 kbar (x = 1, black 1160 star in Figure 13). $X_{added melt}$ is the proportion of melt added in the migmatitic orthogneiss at 16 1161 kbar. x = 1 corresponds to 20 mol. % of melt added. The solidus is underlined by a thick black 1162 dashed line. The calculated isopleths show molar proportion of garnet (g mol. %), almandine 1163 (x(alm)) and grossular (z(grs)) content of garnet, Si content of white micas (Si(wm) p.f.u.) 1164 and molar proportion of melt (liq mol. %). The ellipses indicate the *P*–*T* ranges compatible 1165 with the observed assemblage and core and rim compositions of garnet and white mica. 1166 Evolution along three decompression paths at different $X_{added melt}$ is discussed in the text.

Fig. 15. (a) *P*–*T* pseudosection calculated with 3.40 mol. % melt added to the whole-rock composition of the nebulitic orthogneiss. (b–e) Simplified pseudosections with compositional isopleths of spessartine (m(sps)), almandine (x(alm)) and grossular (z(grs)) in garnet; Si content of muscovite (Si(wm) p.f.u.); anorthite content of plagioclase (ca(pl)); and molar proportion of melt (liq (mol. %)). The ellipses indicate the *P*–*T* ranges compatible with the observed assemblage and core and rim compositions of garnet and white mica. The solidus is underlined by a thick black dashed line. See text for discussion of the *P*–*T* path.

1174 Fig. 16. Sketches summarizing the variations of different textural parameters and melt loss-1175 gain relationship as indicated by geochemical signatures (REE - Rare Earth Elements; HFSE 1176 - High Field Strength Element) across both antiforms. (a) Miedzygórze antiform: melt-absent 1177 orthogneiss with local migmatite formation. Shallow-dipping S1 fabric preserved in the low-1178 strain D2 domains. Grain-scale melt percolation is mainly localized in narrow zones of 1179 vertical S2 fabric (modified after Štípská et al. 2019). Compilation of P-T paths for 1180 orthogneiss reported by Chopin et al. (2012b) (1), and Štípská et al. (2019) (2). (b) Králíky-1181 Śnieżnik antiform: melt-present migmatitic orthogneiss. High-strain D2 domains with 1182 subvertical S2 foliation are connected with crustal-scale shear zones. The wide zone of 1183 subvertical S2 fabric is to a large extent percolated by melt. Simplified P-T diagram with the 1184 P-T path obtained in this study. P-T paths are mostly within the melt-present assemblages.

(c) Tectonic sketch of the Orlica-Śnieżnik Dome as a part of the Sudetes showing shallowdipping S1 fabrics related to subduction of the continental crust up to eclogite- and (U)HP
granulite-facies conditions, and subvertical S2 fabrics related to its vertical exhumation to the
middle and upper crust (modified after Chopin et al. 2012a). The positions in subduction
wedge of two antiforms are indicated as a proximal part (a) and a more distal part (b) with
respect to the subduction.

- **Table 01.** Representative analyses of feldspar.
- **Table 02.** Representative analyses of micas.
- **Table 03.** Representative analyses of garnet.
- **Table 04.** Major and trace-element compositions (ICP-AES and -MS). LOI: Loss On Ignition.
- Table 05. Gain/loss of incompatible elements of the studied rocks relative to weakly
 migmatized banded type II orthogneiss (sample FC076A).